thank the SDSC for a grant of computer time.

Note Added in Proof. As we received the proofs of this manuscript, we also received a manuscript from Prof. K. P. C. Vollhardt on the structure of **6**. The low-temperature X-ray structure of **6** reveals an exo bond length of 1.390 Å and an endo bond length of 1.413 Å (δ = 2.3 pm) (Haley M. M.; Mohler, D. L.; Blăser, D.; Boese, R.; Vollhardt, K. P. C., manuscript in preparation.) These results agree well with our predictions. We thank Prof. Vollhardt for providing us with access to this data.

Supplementary Material Available: Tables of bond lengths and bond angles and torsions (2 pages). Ordering information is given on any current masthead page.

Analogies between the Concepts of Molecular Chemistry and Solid-State Physics concerning Structural Instabilities. Electronic Origin of the Structural Modulations in Layered Transition-Metal Dichalcogenides

Myung-Hwan Whangbo*,† and Enric Canadell*,‡

Contribution from the Department of Chemistry, North Carolina State University, Raleigh, North Carolina 27695-8204, and Laboratoire de Chimie Théorique, Université de Paris-Sud, 91405 Orsay, France. *Received June 8, 1992*

Abstract: The concepts of both Fermi surface nesting and local chemical bonding were employed to analyze the electronic origin of the structural modulations of layered transition-metal dichalcogenides 1T-MX_2 and 2H-MX_2. Analogies between the two concepts and their complementary nature were examined. The concept of hidden Fermi surface nesting was used to explain the d-electron-count dependence of the structural modulations of the 1T-MX_2 layers containing $d^{4/3}$, d^2, and d^3 ions on the basis of their hidden one-dimensional Fermi surfaces. The latter are derived from the observations that these layers are made up of three different sets of edge-sharing octahedral chains and that strong σ-bonding interactions between the t_{2g} orbitals occur along each chain direction. From the viewpoint of local chemical bonding, the driving force for the diamond-chain formation in the d^3 systems and the zigzag-chain formation in the d^2 systems is two-center, two-electron σ-bonding, but that for the ribbon-chain formation in the $d^{4/3}$ systems is three-center, two-electron σ-bonding. Several structural modulations of 1T-MX_2 and 2H-MX_2 layers, difficult to understand in terms of Fermi surface nesting, were examined by performing molecular orbital and tight-binding band electronic structure calculations. The $\sqrt{13} \times \sqrt{13}$ modulation of a d^1 1T-MX_2 layer is described as a superposition of linear, multicenter σ-bonding interactions which occur in three different directions around metal atoms. The 2 × 2 modulation of 1T-$TiSe_2$ results from a second-order Jahn–Teller instability of the $TiSe_6$ octahedra with d^0 ions. The 3 × 3 modulation of a d^1 2H-MX_2 layer occurs to enhance the extent of the metal–metal bonding interactions between adjacent MX_6 trigonal prisms. Structural modulations arising from Fermi surface nesting in low-dimensional metals are equivalent in nature to first-order Jahn–Teller distortions of molecules. Structural modulations of low-dimensional metals do not always originate from Fermi surface nesting, just as not all molecular distortions are caused by first-order Jahn–Teller distortions.

1. Introduction

Since the seminal work by Wilson, DiSalvo, and Mahajan[1] and by Williams, Parry, and Scruby[2] in the early 1970s on transition-metal dichalcogenides,[3] charge density wave (CDW) phenomena have become an important topic to study. Over the years, the research field of CDW phenomena has grown tremendously to include other transition-metal chalcogenides, transition-metal oxides, and organic charge-transfer salts.[4]

The CdI_2-type transition-metal dichalcogenides, 1T-MX_2 (M = transition metal; X = S, Se, or Te), consist of MX_2 layers obtained from MX_6 octahedra by sharing their edges (Figure 1a).[5] The metal atoms of an undistorted MX_2 layer form a hexagonal lattice (Figure 1b); this is observed for 1T-TiS_2, which contains d^0 ions. The 1T-MX_2 phases with d-electron counts from d^1 to d^3 exhibit various patterns of structural distortions resulting from their metal–metal bonding: The 1T-MX_2 (M = Ta, X = S or Se) systems, which have d^1 ions, exhibit a $\sqrt{13} \times \sqrt{13}$ metal-atom clustering (Figure 1c). The 1T-MTe_2 (M = V, Nb, or Ta) systems, for which the d-electron count is formally d^1 but actually close to $d^{4/3}$ because of a partial chalcogen-to-metal electron transfer,[6] have their metal ions clustered into "ribbon-chains" (Figure 1d). The metal ions of the 1T-MX_2 phases with d^2 electron count show "zigzag-chains" (Figure 1e), while those with d^3 electron count exhibit "diamond-chains" (Figure 1f). Thus the metal–metal bonding patterns of 1T-MX_2 phases depend critically

† North Carolina State University.
‡ Université de Paris-Sud.

(1) (a) Wilson, J. A.; DiSalvo, F. J.; Mahajan, S. *Phys. Rev. Lett.* **1974**, *32*, 882. (b) Wilson, J. A.; DiSalvo, F. J.; Mahajan, S. *Adv. Phys.* **1975**, *24*, 117.

(2) (a) Williams, P. M.; Parry, G. S.; Scruby, C. B. *Philos. Mag.* **1974**, *29*, 695. (b) Williams, P. M. In *Crystallography and Crystal Chemistry of Materials with Layered Structures*; Lévy, F., Ed.; Reidel: Dordrecht, The Netherlands, 1976; Vol. 2, p 51.

(3) For early reviews, see: (a) Wilson, J. A.; Yoffe, A. D. *Adv. Phys.* **1969**, *18*, 193. (b) Hulliger, F. *Struct. Bonding (Berlin)* **1967**, *4*, 83.

(4) For representative reviews, see: (a) *Electronic Properties of Inorganic Quasi-One-Dimensional Compounds*; Monceau, P., Ed.; Reidel: Dordrecht, The Netherlands, 1985; parts I and II. (b) *Crystal Chemistry and Properties of Materials with Quasi-One-Dimensional Structures*; Rouxel, J., Ed.; Reidel: Dordrecht, The Netherlands, 1986. (c) *Structure Phase Transitions in Layered Transition Metal Compounds*; Motizuki, K., Ed.; Reidel: Dordrecht, The Netherlands, 1986. (d) *Low-Dimensional Electronic Properties of Molybdenum Bronzes and Oxides*; Schlenker, C., Ed.; Kluwer Academic Publishers: Dordrecht, The Netherlands, 1989. (e) Pouget, J. P. In *Semiconductors and Semimetals*; Conwell, E., Ed.; Academic Press: New York, 1988; Vol. 27, p 87. (f) Friend, R. H.; Jérome, D. *J. Phys. C: Solid State Phys.* **1979**, *12*, 1441. (g) Friend, R. H.; Yoffe, A. D. *Adv. Phys.* **1987**, *36*, 1. (h) Withers, R. L.; Wilson, J. A. *J. Phys. C: Solid State Phys.* **1986**, *19*, 4809.

(5) Hulliger, F. In *Structural Chemistry of Layer-Type Phases*; Lévy, F., Ed.; Reidel: Dordrecht, The Netherlands, 1976.

(6) Canadell, E.; Jobic, S.; Brec, R.; Rouxel, J.; Whangbo, M.-H. *J. Solid State Chem.* **1992**, *99*, 189.

0002-7863/92/1514-9587$03.00/0

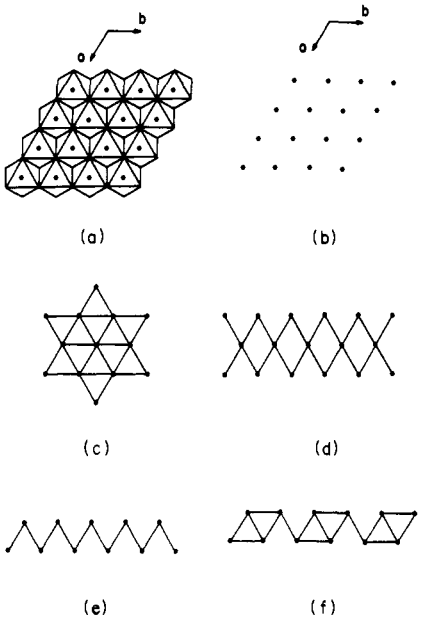

Figure 1. (a) Schematic projection view of an undistorted 1T-MX_2 layer along the c-direction (perpendicular to the layer). (b) Metal ion arrangement in an undistorted 1T-MX_2 layer. (c) $\sqrt{13} \times \sqrt{13}$ clustering of metal atoms in 1T-MX_2 with d^1 ions. (d) Ribbon-chain clustering of metal atoms in 1T-MX_2 with $d^{4/3}$ ions. (e) Zigzag-chain clustering of metal atoms in 1T-MX_2 with d^2 ions. (f) Diamond-chain clustering of metal atoms in 1T-MX_2 with d^3 ions.

on the metal d-electron count. Formation of such metal–metal bonds as found for the 1T-MX_2 layers containing d^1 to d^3 ions does not occur in 1T-TiX_2 (X = S, Se, or Te), but 1T-$TiSe_2$ exhibits a 2×2 structural modulation (section 6) while such a modulation is absent in 1T-TiS_2 and 1T-$TiTe_2$. Another interesting distortion pattern observed for transition-metal dichalcogenides is the 3×3 modulation found in the 2H-MX_2 (M = Nb, X = Se; M = Ta, X = S or Se) layers with d^1 ions, which are constructed from MX_6 trigonal prisms (section 7). In the past nearly two decades, a number of theoretical studies[4c,7] have been carried out to explain these structural modulations in the transition-metal dichalcogenides, and yet a satisfactory understanding of the electronic origin of these modulations has remained elusive.

The electronic instabilities of molecules causing their structural distortions are generally described in terms of Jahn–Teller distortion, a concept of molecular chemistry.[8] On the other hand, the electronic instabilities of low-dimensional metals leading to their structural modulations are often discussed in terms of Fermi surface nesting,[1b] a concept of solid-state physics. In certain ways, these concepts of molecular chemistry and solid-state physics should be similar, and complementary as well, because, after all, extended solids are giant molecules. A CDW phenomenon is found typically for one-dimensional (1D) metals, but it is also observed for certain two-dimensional (2D) metals such as the Magnéli phase Mo_4O_{11}, the monophosphate tungsten bronzes, and the purple bronzes AMo_6O_{17} (A = K, Na, or Tl).[4d] The need to explain this seemingly unusual finding gave rise to the concept of hidden Fermi surface nesting (hereafter, referred to as hidden nesting),[9] which is formulated from the recognition that the partially filled bands of the 2D layers of corner-sharing MO_6 (M = Mo or W) octahedra, present in these materials, can be decomposed into contributions of different sets of 1D chains of corner-sharing MO_6 octahedra. The MX_2 layers of the 1T-MX_2 phases are derived

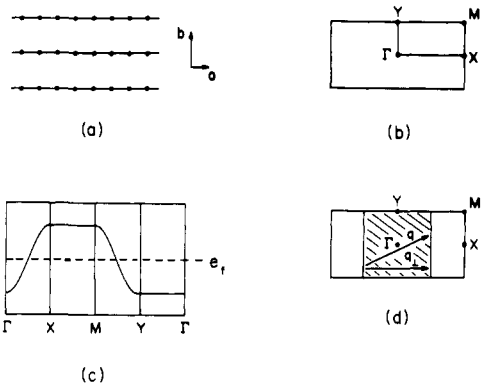

Figure 2. (a) Schematic representation of a rectangular 2D lattice. (b) FPZ associated with the rectangular 2D lattice in Figure 2a. Γ = (0, 0), X = ($a^*/2$, 0), Y = (0, $b^*/2$), and M = ($a^*/2$, $b^*/2$). (c) Dispersion relations expected when the 2D lattice of Figure 1 has no intersite interaction along the b-direction. The dashed line represents the Fermi level. (d) Occupied wave vectors (shaded) and unoccupied wave vector (unshaded) of the FPZ associated with the half-filled band of Figure 2c. The Fermi surface consists of two parallel lines, perpendicular to the chain direction, separated by the distance of $q_\perp = a^*/2$.

from MX_6 octahedra by edge-sharing, so that direct metal–metal interactions are strong unlike the case of the layers of corner-sharing octahedra. Nevertheless, as will be shown in our work, the concept of hidden nesting can be used to explain the structural modulations of the 1T-MX_2 phases containing $d^{4/3}$, d^2, and d^3 ions. However, the $\sqrt{13} \times \sqrt{13}$ modulation of 1T-MX_2 (M = Ta, X = S or Se; M = V, X = Se), the 2×2 modulation of 1T-$TiSe_2$, and the 3×3 modulation of 2H-MX_2 (M = Nb, X = Se; M = Ta, X = S or Se) are difficult to understand from the viewpoint of Fermi surface nesting.

In the present work, we analyze the electronic origin of the structural modulations in the transition-metal dichalcogenides 1T-MX_2 and 2H-MX_2 on the basis of the electronic structures of their undistorted MX_2 layers and also examine analogies between the concepts of molecular chemistry and solid-state physics concerning electronic instability and structural distortion. To achieve these objectives, we carry out extended Hückel tight-binding (EHTB) band electronic structure calculations[10] for various MX_2 layers and also extended Hückel molecular orbital (EHMO) calculations[11] for appropriate molecular clusters. The atomic parameters employed in our study were taken from previous works.[6,12]

Our work is organized as follows: Section 2 briefly summarizes several solid-state physics concepts and terminologies needed in our discussion. In section 3, we describe the t_{2g}-block bands and the Fermi surfaces calculated for an undistorted 1T-MX_2 layer and then examine how these bands can be decomposed into contributions of the edge-sharing octahedral chains constituting the MX_2 layer. In section 4, the structural modulations found for the 1T-MX_2 layers containing d^3, d^2, and $d^{4/3}$ ions are explained in terms of hidden nesting, and the alternative explanations based on chemical bonding are discussed. The $\sqrt{13} \times \sqrt{13}$ structural modulations of 1T-MX_2 containing d^1 ions are separately discussed in section 5. We examine why 1T-$TiSe_2$ has a particular structural modulation while 1T-TiS_2 and 1T-$TiTe_2$ do not in section 6. The cause for the 3×3 modulation of 2H-MX_2 is analyzed in section 7. Finally, we summarize important findings of our work in section 8.

2. Fermi Surface Nesting, CDW Modulation, and Related Concepts

The structural modulations of low-dimensional metals (e.g., 1T- and 2H-MX_2 phases) are mostly discussed in terms of the concepts

(7) Doni, E.; Girlanda, R. In *Electronic Structure and Electronic Transitions in Layered Materials*; Grasso, V., Ed.; Reidel: Dordrecht, The Netherlands, 1986; p 1.

(8) (a) Salem, L. *The Molecular Orbital Theory of Conjugated Systems*; Benjamin: New York, 1966. (b) Albright, T. A.; Burdett, J. K.; Whangbo, M.-H. *Orbital Interactions in Chemistry*; Wiley: New York, 1985.

(9) (a) Whangbo, M.-H.; Canadell, E.; Foury, P.; Pouget, J. P. *Science* **1991**, *252*, 96. (b) Canadell, E.; Whangbo, M.-H. *Chem. Rev.* **1991**, *91*, 965.

(10) Whangbo, M.-H.; Hoffmann, R. *J. Am. Chem. Soc.* **1978**, *100*, 6093.

(11) Hoffmann, R. *J. Chem. Phys.* **1963**, *39*, 1397.

(12) Canadell, E.; Rachidi, I. E.-I.; Pouget, J. P.; Gressier, P.; Meerchaut, A.; Rouxel, J.; Jung, D.; Evain, M.; Whangbo, M.-H. *Inorg. Chem.* **1990**, *29*, 1401.

and terminologies developed in solid-state physics, which are unfamiliar to most chemists. To facilitate our discussion of the analogies between the concepts of molecular chemistry and solid-state physics dealing with structural instabilities, we briefly describe several concepts and terminologies of solid-state physics in this section. (For more detailed discussions, see ref 9b.)

A. Band Dispersion and Wave Vector. For simplicity, we consider a rectangular 2D lattice with repeat vectors **a** and **b** shown in Figure 2a. Without loss of generality, each lattice site may be assumed to have one orbital and one electron. Under the approximation of nearest-neighbor interactions and with the neglect of overlap integrals, the energies allowed for the 2D lattice are written as $e(k_a,k_b) = \alpha + 2\beta_a \cos(k_a a) + 2\beta_b \cos(k_b b)$. Here α is the energy of the site orbital, and β_a and β_b are the nearest-neighbor resonance integrals along the a- and b-directions, respectively. The wave vectors $\mathbf{k} \equiv (k_a, k_b)$ can have any value of the first primitive zone (FPZ) (see Figure 2b) defined by $-a^*/2 \leq k_a \leq a^*/2$ and $-b^*/2 \leq k_b \leq b^*/2$, where $a^* = 2\pi/a$ and $b^* = 2\pi/b$. For the rectangular 2D lattice, the directions of the reciprocal vectors **a*** and **b*** are the same as those of the repeat vectors **a** and **b**, respectively.

Suppose that the 2D lattice represents an ideal 1D system so that $\beta_a \neq 0$ and $\beta_b = 0$. That is, there is no intersite interaction along the b-direction, and so the 2D lattice is an assembly of noninteracting chains running along the a-direction. Then, the $e(\mathbf{k})$ vs **k** plot is dispersive along the chain direction but dispersionless along the interchain direction, as illustrated in Figure 2c. With one electron per site, the bottom halves of the allowed energy levels are each doubly occupied to form a metallic state. The dashed line of Figure 2c represents the highest occupied level, i.e., the Fermi level e_f.

B. Fermi Surface Nesting. The wave vectors of the FPZ associated with the occupied and unoccupied levels of a partially filled band are commonly called the occupied and unoccupied wave vectors, respectively. The Fermi surface of a partially filled band is the boundary surface separating the occupied wave vectors from the unoccupied wave vectors in the FPZ. For the wave vectors on the Fermi surface, denoted by $\mathbf{k}_f$, one finds $e(\mathbf{k}_f) = e_f$. Figure 2d shows the regions of the occupied and unoccupied wave vectors associated with the half-filled band of Figure 2c. It is clear that the Fermi surface of this half-filled band consists of two parallel lines perpendicular to the chain direction. In a 2D representation (i.e., in a representation where the energies are expressed in terms of two independent wave vectors, e.g., k_a and k_b), an ideal 1D metal has a Fermi surface consisting of two parallel lines perpendicular to the chain direction. A 2D metal has a Fermi surface consisting of closed loops in a 2D representation.

When a piece of a Fermi surface is superimposed on another piece of the Fermi surface by a translational vector **q**, the Fermi surface is said to be nested by the vector **q**. The Fermi surface in Figure 2d has an infinite number of nesting vectors, all of which can be written as a sum of two orthogonal components, i.e., $\mathbf{q} = q_\perp + q_\parallel$. Here $q_\perp$ and $q_\parallel$ are perpendicular and parallel to the Fermi surface, respectively. When the Fermi vectors $\mathbf{k}_f$ of Figure 2d are written as $\mathbf{k}_f = (\pm k_f, k_b)$, the distance between the two parallel lines of the 1D Fermi surface is given by $q_\perp = 2k_f$.

C. CDW and Electron Counting. In general, a 1D metal with a Fermi surface nested by a vector **q** is susceptible to form a CDW state. The latter induces a structural modulation into the lattice, whose periodicity is described by the function cos (**q**·**R**), where **R** represents the lattice points $m\mathbf{a} + n\mathbf{b}$ (m, n = integers). In diffraction measurements, in which reflection intensities are recorded in reciprocal space, the Bragg reflection gives rise to the reciprocal lattice points $m\mathbf{a}^* + n\mathbf{b}^*$ (m, n = integers), and the reflection arising from the CDW leads to diffuse lines or lines of diffuse spots, which are perpendicular to the chain direction at the distance $q_\perp$ from the reciprocal lattice points.[13]

The electronic energy gain associated with a CDW increases when more electrons are involved in the CDW formation. Thus, the larger the area of the nested Fermi surface (the length in the case of a 2D representation) is, the stronger the tendency for the associated CDW formation becomes. An important manifestation of this fact is that a system with two different sets of 1D Fermi surfaces typically undergoes a CDW formation with a single nesting vector common to both sets.[14] An important consequence of CDW formation is the opening of a band gap at the Fermi level, so that CDW formation typically induces a metal–insulator phase transition.

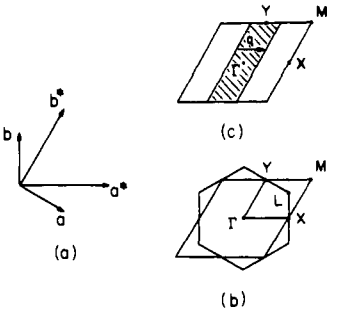

Figure 3. (a) Relationship between the repeat vectors (**a** and **b**) of the hexagonal lattice in Figure 1a and the associated reciprocal lattice vectors (**a*** and **b***). (b) FPZ (rhombus) and FBZ (regular hexagon) associated with the hexagonal lattice of Figure 1. $\Gamma = (0, 0)$, $X = (a^*/2, 0)$, $Y = (0, b^*/2)$, $M = (a^*/2, b^*/2)$, and $L = (a^*/3, b^*/3)$. (c) Occupied wave vectors (shaded) and unoccupied wave vector (unshaded) of the FPZ expected when the hexagonal lattice of Figure 1a has no intersite interactions along the b-direction and when the resulting band is one-third-filled. The Fermi surface consists of two parallel lines perpendicular to the chain direction (i.e., a-direction), and $\mathbf{q} = \mathbf{a}^*/3$.

For a partially filled band, the area of the occupied wave vector region in the FPZ is proportional to the band occupancy, f. For instance, in Figure 2d, half the FPZ is occupied. For a partially filled, ideal 1D band associated with chains running along the a-direction, the band occupancy f is given by $f = q_\perp/a^*$, which is an observable quantity in diffraction measurements. From this relationship and the function cos (**q**·**R**) describing the CDW modulation, it is found that, for commensurate values of $q_\perp$, for which f is a simple fraction $1/n$ (n = 2, 3, 4, etc.), the CDW modulation increases the lattice periodicity by n-fold along the chain direction (e.g., the direction perpendicular to the 1D Fermi surface). In general, when a nesting vector **q** of a 1D Fermi surface is given by a $1/n$ fraction of a reciprocal-space vector (even for cases when the reciprocal vectors **a*** and **b*** are not orthogonal to each other), then the associated CDW increases the lattice periodicity n-fold along the direction perpendicular to the Fermi surface (i.e., the chain direction). This arises from the fact that the periodicity of a CDW is described by the function cos (**q**·**R**), and that $\mathbf{a}\cdot\mathbf{a}^* = \mathbf{b}\cdot\mathbf{b}^* = 2\pi$, and $\mathbf{a}\cdot\mathbf{b}^* = \mathbf{b}\cdot\mathbf{a}^* = 0$.

D. Unit Cell. Unlike the case of the rectangular lattice of Figure 2a, the repeat vectors **a** and **b** of the MX_2 layer make an angle of 120° (Figure 1a). The reciprocal vectors **a*** and **b*** must be perpendicular to **b** and **a**, respectively, so that the vectors **a*** and **b*** make an angle of 60° (see Figure 3a). As a unit cell of the reciprocal space, it is common to use the first Brillouin zone (FBZ) rather than the FPZ for symmetry reasons, although use of either one is equally valid. (In our later discussion of any Fermi surface, it is important to recall that the overall pattern generated by repeating the surface presented in a chosen unit cell is what really matters.) The FBZ and FPZ are identical for the rectangular lattice, but this is not the case for the hexagonal lattice.[9b] As also shown in Figure 3b, the FBZ of the hexagonal lattice is a regular hexagon. In the present work, the FPZ is employed for the discussion of the 1T-MX_2 and 2H-MX_2 layers.

Finally, we consider the electron counting on the basis of the FPZ of a hexagonal lattice. Suppose that a "hexagonal" lattice consists of 1D chains running along the a-direction, and this lattice leads to a one-third-filled 1D band. As shown in Figure 3c, the

(13) Moret, R.; Pouget, J. P. in ref 4b, p 87.

(14) (a) Pouget, J. P.; Noguera, C.; Moudden, A. H.; Moret, R. *J. Phys. (Paris)* **1985**, *46*, 1731. (b) Whangbo, M.-H.; Schneemeyer, L. F. *Inorg. Chem.* **1986**, *25*, 2424.

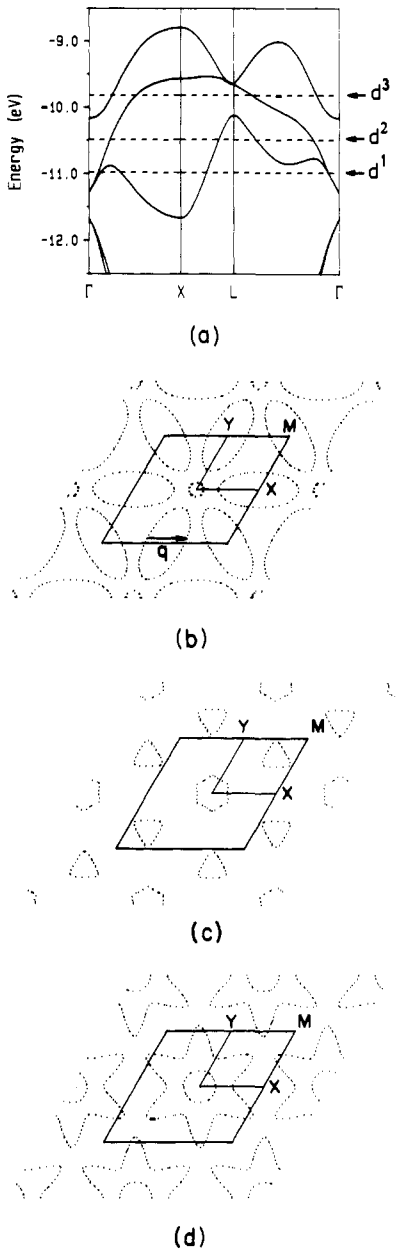

Figure 4. (a) Dispersion relations of the t_{2g}-block bands of an undistorted 1T-MX_2 layer calculated on the basis of the undistorted 1T-TaS_2 layer. The three dashed lines refer to the Fermi levels corresponding to the d^1, d^2, and d^3 electron counts. $\Gamma = (0, 0)$, $X = (a^*/2, 0)$, and $L = (a^*/3, b^*/3)$. (b) Fermi surface of an undistorted 1T-MX_2 layer with d^1 ions calculated on the basis of the t_{2g}-block bands of Figure 4a. $X = (a^*/2, 0)$, $Y = (0, b^*/2)$, and $M = (a^*/2, b^*/2)$. The vector $\mathbf{q} \simeq 0.31\mathbf{a}^*$ is a partial nesting vector. (c) Fermi surface of an undistorted 1T-MX_2 layer with d^2 ions calculated on the basis of the t_{2g}-block bands of Figure 4a. (d) Fermi surface of an undistorted 1T-MX_2 layer with d^3 ions calculated on the basis of the t_{2g}-block bands of Figure 4a.

Fermi surface for this case consists of parallel lines perpendicular to the chain direction (i.e., a-direction). The nesting vector $\mathbf{q}$ shown in Figure 3c is parallel to $\mathbf{a}^*$ with the length $q = a^*/3$.

3. Electronic Structure of an Ideal 1T-MX_2 Layer

A. t_{2g}-Block Bands and Fermi Surfaces. We now survey the t_{2g}-block band structure and the associated Fermi surfaces of an undistorted MX_2 layer. Figure 4a shows the t_{2g}-block bands calculated for a single TaS_2 layer on the basis of the undistorted 1T-TaS_2 structure[5] by performing EHTB calculations. The three dashed lines are the Fermi levels corresponding to the d-electron counts of d^1, d^2, and d^3. The Fermi surfaces calculated for these d-electron counts are shown in Figure 4b–d, which agree well with those obtained by first-principles calculations.[7] What is most striking is that nesting is poor, if present at all, in all the three Fermi surfaces. Thus, by applying the concept of nesting to such Fermi surfaces as obtained from band electronic structure calculations, it is obviously difficult to understand the d-electron-count dependence of the structural modulations found for the 1T-MX_2 phases.

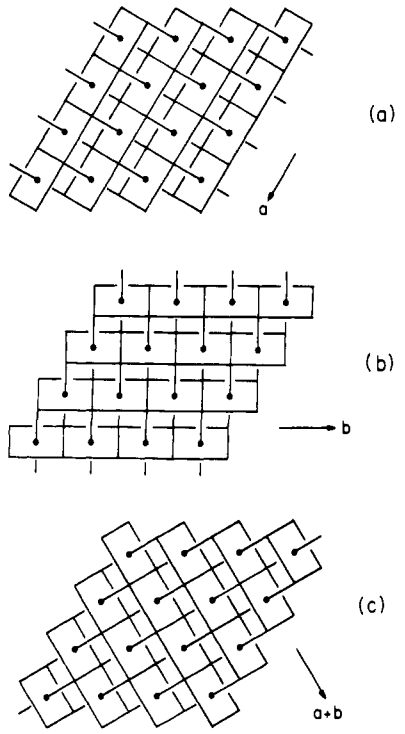

Figure 5. Decomposition of an undistorted 1T-MX_2 layer into sets of edge-sharing octahedral chains running along: (a) the a-direction, (b) the b-direction, and (c) the $(a + b)$-direction.

B. Edge-Sharing Octahedral Chains of a 1T-MX_2 Layer. The topological aspects of the Fermi surfaces of Figure 4b–d may now be considered. The ideal MX_2 layer of Figure 1a is constructed from edge-sharing octahedral chains running along the a-, b-, or $(a + b)$-directions, as shown in Figure 5a–c. For the convenience of our discussion, the plane containing the shared edges of MX_6 octahedra will be referred to as the equatorial plane, and the t_{2g} orbital contained in the equatorial plane (see **1**) as the in-plane t_{2g} orbital. Then, each MX_6 octahedron possesses three equatorial

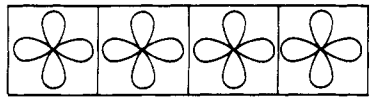

1

planes and three corresponding in-plane t_{2g} orbitals. Given a set of edge-sharing octahedral chains parallel to the a-, b-, or $(a + b)$-directions, the metal–metal interactions resulting from their in-plane t_{2g} orbitals are strong within each chain, being σ in character (see **1**), but weak between adjacent chains, being pseudo-δ in nature.

C. Hidden 1D Fermi Surface. If we consider only the interactions between the in-plane t_{2g} orbitals within each chain, then the t_{2g}-block bands of an ideal 1T-MX_2 layer are simply a superposition of the three independent 1D bands (see Figure 6a) resulting from the corresponding in-plane t_{2g} orbitals. Suppose for an MX_2 layer containing d^n ions that the d electrons are equally shared among the three independent 1D bands. Then, the occupancy of each 1D band is given by $f = n/6$. Thus, the three independent 1D bands are each one-sixth-, one-third-, and one-half-filled for the d^1, d^2, and d^3 1T-MX_2 systems, respectively, as shown in Figure 6b–d. The superposed 1D Fermi surfaces expected for the d^1, d^2, and d^3 electron counts are shown in Figure 7a–c, respectively. [Note that each Fermi surce (i.e., each set

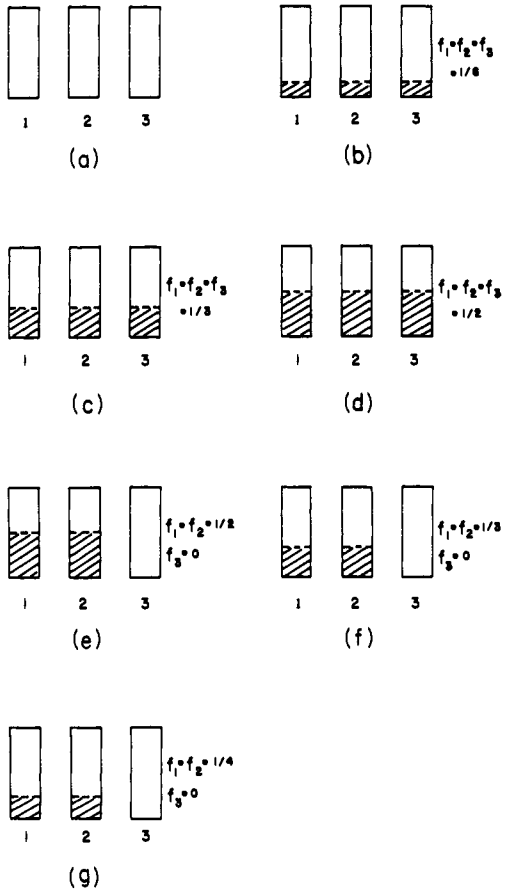

Figure 6. Schematic representations of the three hidden 1D bands comprising the t_{2g}-block bands of an undistorted 1T-MX_2 layer and their band occupancies: (a) Three hidden 1D bands. (b) Three one-sixth-filled 1D bands expected for a d^1 1T-MX_2 system. (c) Three one-third-filled 1D bands expected for a d^2 1T-MX_2 system. (d) Three one-half-filled 1D bands expected for a d^3 1T-MX_2 system. (e) Two one-half-filled 1D bands and an empty band expected for a d^2 1T-MX_2 system. (f) Two one-third-filled 1D bands and an empty band expected for a $d^{4/3}$ 1T-MX_2 system. (g) Two one-fourth-filled 1D bands and an empty band expected for a d^1 1T-MX_2 system.

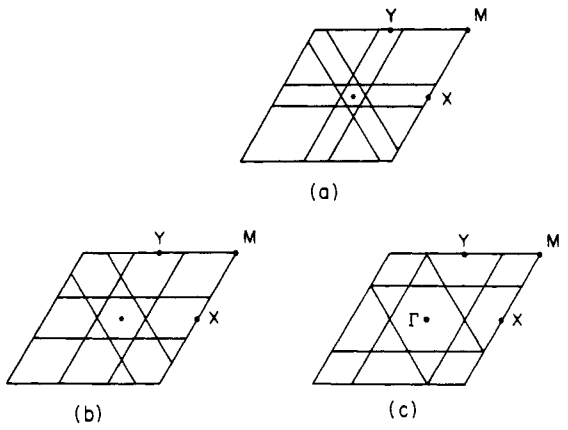

Figure 7. Hidden 1D Fermi surfaces associated with the following: (a) the three one-sixth-filled bands of Figure 6b, (b) the three one-third-filled bands of Figure 6c, and (c) the three one-half-filled bands of Figure 6d.

of parallel lines) is perpendicular to one of the three chain directions of the 1T-MX_2 layer (i.e., the *a*-, *b*-, and (*a* + *b*)-directions) in Figure 5.] Such superposed 1D Fermi surfaces will be referred to as hidden 1D Fermi surfaces.

The calculated and the hidden 1D Fermi surfaces have almost no resemblance for the d^2 electron count (Figure 4c vs Figure 7b) but some resemblance for the d^1 and d^3 electron counts (Figure 4b vs Figure 7a and Figure 4d vs Figure 7c). The primary cause

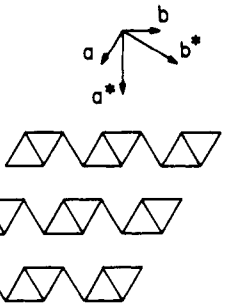

Figure 8. Schematic representation of the diamond-chain pattern in a 1T-MX_2 layer with d^3 ions. Note that, with respect to the undistorted lattice, the diamond-chain formation amounts to a dimerization along the *a*-, *b*-, and (*a* + *b*)-directions.

for the poor resemblance between the calculated and the hidden 1D surfaces is the metal–metal interactions involving the in-plane t_{2g} orbitals contained in nonparallel equatorial planes. Such direct metal–metal interactions, certainly present in the undistorted structure of 1T-MX_2, are likely to become strongly weakened when structural modulations are introduced into the lattice, because the MX_6 octahedra are distorted by the modulations. Under this circumstance, which we believe is applicable to the 1T-MX_2 systems, it is justified to use the hidden 1D Fermi surfaces in discussing the structural modulations of 1T-MX_2.

It should be emphasized that the importance of σ-bonding interactions involving the in-plane t_{2g} orbitals in CdI_2-type layers has been recognized for some years. Notably, Inglesfield[15] considered the topologies of the calculated Fermi surfaces of 1T-MX_2 in terms of the hidden 1D Fermi surfaces, while Burdett and Hughbanks[16] discussed several patterns of metal-atom clustering in CdI_2-type transition-metal oxide layers from the viewpoint of two-center, two-electron σ-bonding.

4. Hidden Nesting and CDW Modulation

The structural modulations observed for the 1T-MX_2 systems containing d^3, d^2, and $d^{4/3}$ ions are analyzed in this section. We examine how the d-electron-count dependence of these structural modulations can be understood by employing the hidden nesting concept and also by employing the concept of local chemical bonding. Our discussion shows that both approaches are equivalent.

A. 1T-MX_2 Layers of d^3 ions.[17] With d^3 ions, the t_{2g} levels of each MX_6 octahedron of a 1T-MX_2 layer can each accommodate one electron. The σ-interactions between two adjacent in-plane t_{2g} orbitals lead to the two molecular orbitals **2a**,**b**. Thus,

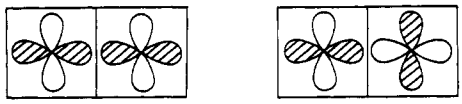

2a **2b**

by assuming that each in-plane t_{2g} orbital is used to form the two-center, two-electron σ-bonding level **2a**, one can generate several patterns[16] of metal-atom clustering including the diamond-chains shown in Figure 8. The latter pattern is found in several layered compounds containing d^3 ions, which include ReX_2 (X = S or Se)[18a,b] and $M'Mo_2S_4$ (M' = V, Cr, Fe, or Co.)[18c]

Let us examine how the formation of the diamond-chain pattern can be explained on the basis of the hidden 1D Fermi surfaces found for the d^3 electron count (Figure 7c). The three sets of 1D Fermi surfaces provide the three nesting vectors $\mathbf{q}_a = \mathbf{a}^*/2$, $\mathbf{q}_b = \mathbf{b}^*/2$, and $\mathbf{q}_{a+b} = (-\mathbf{a}^* + \mathbf{b}^*)/2$, each of which is a common nesting

(15) Inglesfield, J. E. *J. Phys. C: Solid State Phys.* **1980**, *13*, 17.
(16) Burdett, J. K.; Hughbanks, T. *Inorg. Chem.* **1985**, *24*, 1741.
(17) (a) Canadell, E.; LeBeuze, A.; Khalifa, M. A. E.; Chevrel, R.; Whangbo, M.-H. *J. Am. Chem. Soc.* **1989**, *111*, 3778. (b) Kertesz, M.; Hoffmann, R. *J. Am. Chem. Soc.* **1984**, *106*, 3453.
(18) (a) Alcock, N. W.; Kjekshus, A. *Acta Chem. Scand.* **1965**, *19*, 79. (b) Wildervanck, J. C.; Jellinek, F. *J. Less-Common Met.* **1971**, *24*, 73. (c) Guillevic, J.; Le Marouille, J.-Y.; Grandjean, D. *Acta Crystallogr.* **1974**, *B30*, 111.

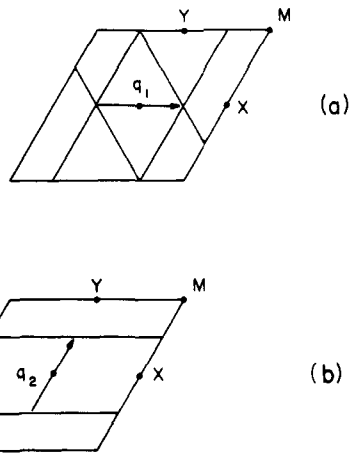

Figure 9. Decomposition of the three hidden 1D Fermi surfaces into (a) the two hidden 1D Fermi surfaces with the common nesting vector $\mathbf{q}_1 = \mathbf{a}^*/2$ and (b) the hidden 1D Fermi surface with the nesting vector $\mathbf{q}_2 = \mathbf{b}^*/2$.

vector for two sets of 1D Fermi surfaces. This situation is identical with that found for the purple bronze KMo_6O_{17},[9] which exhibits CDW fluctuations associated with all three nesting vectors thereby showing that the layers of MoO_6 octahedra in this bronze retain a trigonal symmetry in the CDW state. In contrast, the diamond-chain distortion found for ReX_2 (X = S or Se)[18a,b] and $M'Mo_2S_4$ (M' = V, Cr, Fe, or Co)[18c] (see Figure 8) does not have a trigonal symmetry for the layers of MX_6 octahedra. This can be explained by decomposing the three 1D Fermi surfaces of Figure 7c into two sets of 1D surfaces as shown in Figure 9 parts a and b. The two 1D Fermi surfaces of Figure 9a have the common nesting vector $\mathbf{q}_1 = \mathbf{a}^*/2$, and the single 1D Fermi surface of Figure 9b has the nesting vector $\mathbf{q}_2 = \mathbf{b}^*/2$. The vector $\mathbf{q}_1$ nests the 1D Fermi surface parallel to $\Gamma - Y$, which leads to a dimerization along the direction perpendicular to this Fermi surface (i.e., the a-direction). The vector $\mathbf{q}_1$ also nests the 1D Fermi surface parallel to the $(-a^* + b^*)$-direction. Therefore, it also leads to a dimerization along the direction perpendicular to this Fermi surface [i.e., the (a+b)-direction]. As a consequence, the nesting of the two sets of Fermi surfaces by the common nesting vector $\mathbf{q}_1$ gives rise to the formation of zigzag chains running along the b-direction. Finally, the nesting vector $\mathbf{q}_2 = \mathbf{b}^*/2$ leads to a dimerization along the b-direction, which converts the zigzag chains into the diamond chains.

Why KMo_6O_{17} and the d^3 1T-MX_2 layers respond differently toward the CDW instability given by essentially the same hidden 1D Fermi surfaces lies most likely in their structural differences. The layers of MoO_6 octahedra in KMo_6O_{17} are formed by corner-sharing so that no direct metal–metal bonding is possible, and the CDW instability is accommodated only by weak distortions of the lattice, e.g., tilting motions of the MoO_6 octahedra. Thus, the 1D CDW fluctuations associated with the three nesting vectors $\mathbf{q}_a = \mathbf{a}^*/2$, $\mathbf{q}_b = \mathbf{b}^*/2$, and $\mathbf{q}_{a+b} = (-\mathbf{a}^* + \mathbf{b}^*)/2$ occur with equal strengths.[9a] This is not the case for the 1T-MX_2 layers of MX_6 octahedra. These layers are formed by edge-sharing so that metal–metal distances are short. This allows strong, direct metal–metal bonding through the shared octahedral edges, which provides a way of lowering the energy significantly. To make two-center, two-electron metal–metal bonds, each octahedron distorts to accommodate the bond shortening. Geometrically, it is difficult to form three equivalent two-center, two-electron metal–metal bonds with 3-fold rotational symmetry around each metal center, without severely straining the resulting lattice. However, formation of two such bonds around each metal center, forming the zigzag chains (see below), is easily accommodated. Our explanation based upon Figure 9a,b is equivalent to the statement that the diamond-chain formation is a dimerization of zigzag chains with half-filled bands.[17a]

B. 1T-MX_2 Layers of d^2 and $d^{4/3}$ Ions. The metal clustering pattern of zigzag-chains is observed for the 1T-MX_2 layers containing d^2 ions, which include β-$MoTe_2$,[19a] WTe_2,[19a] α-ZrI_2,[19b] and $M'Nb_2Se_4$ (M' = Ti, V, or Cr).[19c] The structural origin of the differences in the transport properties of these d^2 MX_2 layer systems was studied by EHTB calculations.[20] The metal clustering pattern of zigzag-chains can be explained by employing the concept of two-center, two-electron bonding associated with the σ-interactions between in-plane t_{2g} orbitals,[16] provided that each metal ion uses only two of the three in-plane t_{2g} orbitals.

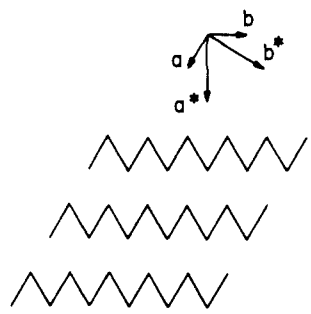

Figure 10. Schematic representation of the zigzag-chain pattern in a 1T-MX_2 layer with d^2 ions. Note that, with respect to the undistorted lattice, the zigzag-chain formation amounts to a dimerization along the a- and $(a + b)$-directions.

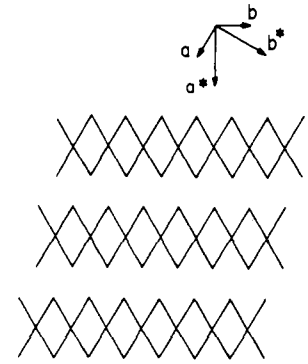

Figure 11. Schematic representation of the ribbon-chain pattern in a 1T-MX_2 layer with $d^{4/3}$ ions. Note that, with respect to the undistorted lattice, the ribbon-chain formation amounts to a trimerization along the a- and $(a + b)$-directions.

We consider how the zigzag-chain formation can be explained in terms of the hidden 1D Fermi surfaces associated with the three independent 1D bands. With d^2 ions, each band becomes one-third-filled (Figure 6c), if the electrons are equally shared among the three bands. The nesting associated with the hidden 1D Fermi surfaces (Figure 7b) predicts a trimerization of the lattice along, for example, the a- and $(a + b)$-directions. This prediction is incompatible with experiment because the zigzag-chain formation (Figure 10) is a dimerization of the lattice with respect to the undistorted lattice. As noted from Figure 9a, a dimerization of the lattice can be achieved by a common nesting vector of two half-filled 1D bands. Consequently, only when two of the three 1D bands are filled with electrons to become each one-half-filled, as depicted in Figure 6e, does one obtain the hidden 1D Fermi surface (such as that given in Figure 9a) responsible for the zigzag-chain formation. Certainly, this unequal band filling, which leads to the best possible utilization of two-center, two-electron metal–metal bonding interactions, breaks the trigonal symmetry of the lattice. Essentially, this description is equivalent to the picture of local chemical bonding in which each metal ion uses only two of the three t_{2g} orbitals in forming the zigzag-chains.

Thus, the concept of hidden nesting becomes more widely applicable in rationalizing structural modulations by allowing for unequal electron distribution among a given set of degenerate

(19) (a) Brown, B. E. *Acta Crystallogr.* **1966**, *20*, 268. (b) Guthrie, D. H.; Corbett, J. D. *J. Solid State Chem.* **1981**, *37*, 256. (c) Meerchaut, A.; Spiesser, M.; Rouxel, J.; Gorochov, O. *J. Solid State Chem.* **1980**, *31*, 31.
(20) Canadell, E.; Whangbo, M.-H. *Inorg. Chem.* **1990**, *29*, 1398.

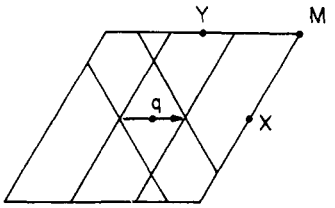

Figure 12. Two hidden 1D Fermi surfaces associated with the two one-third-filled bands of Figure 6f. The common nesting vector $q = a^*/3$ leads to a trimerization of the lattice along the a- and $(a + b)$-directions.

bands. As another example, consider the ribbon-chain formation. With respect to the undistorted lattice, the formation of the ribbon-chains (Figure 11) in 1T-MTe_2 (M = V, Nb, or Ta) is a trimerization of the lattice [e.g., along the a- and $(a + b)$-directions].[21] By analogy with the dimerization predicted from two one-half-filled 1D bands (Figures 6e and 9a), the trimerization can be explained in terms of the common nesting vector associated with two one-third-filled 1D bands (Figures 6f and 12). The d-electron count appropriate for this band filling is $d^{4/3}$, as found for the metal ions of 1T-MTe_2 (M = V, Nb, or Ta).[6] With the formal oxidation state of Te^{2-}, the d-electron count for 1T-MTe_2 (M = V, Nb, or Ta) would be given by d^1. However, our recent study[6] of 1T-VTe_2 strongly suggests that, due primarily to the interlayer Te···Te interactions, the Te p-block bands are raised in energy thereby leading to partial electron transfer from the top portion of the Te p-block bands to the d-block bands of the metal. As a consequence, the actual d-electron count for 1T-VTe_2 is close to $d^{4/3}$.

To explain the ribbon-chain formation in terms of local chemical σ-bonding, we employ the idea of three-center, two-electron σ-bonding. For a linear arrangement of three consecutive metal ions, the σ-interactions of the in-plane t_{2g} orbitals lead to the three molecular orbitals **3a–c**. With two electrons in the most stable

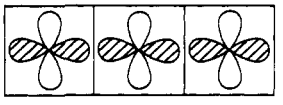

3a

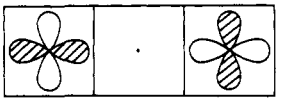

3b

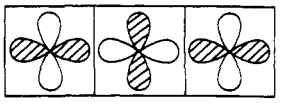

3c

σ-bonding level **3a**, three-center, two-electron σ-bonding is achieved. Then, each ribbon-chain of Figure 11, which has three metal ions per unit cell, is seen to have two three-center, two-electron bonds per unit cell. This means the presence of four electrons per three metal ions, i.e., the d-electron count $d^{4/3}$, in agreement with the description based upon the hidden nesting.

The ribbon-chains of a $d^{4/3}$ 1T-MX_2 system are a "compromise" structural pattern between the $\sqrt{13} \times \sqrt{13}$ clusters of a d^1 1T-MX_2 system and the zigzag-chains of a d^2 1T-MX_2 system. As the d-electron count decreases from d^2 (in other words, as the extent of "electron-deficiency" increases), the tendency for the formation of the clusters based on multicenter two-electron bonding interactions in all three chain directions of the layer increases. So far, our discussion has been concerned only with the metal-atom clustering, not with how the partially filled Te

(21) (a) Bronsema, K. D.; Bus, J. W.; Wiegers, G. A. *J. Solid State Chem.* **1984**, *53*, 415. (b) Brown, B. E. *Acta Crystallogr.* **1966**, *20*, 264.

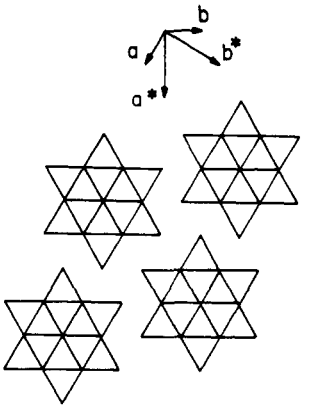

Figure 13. Schematic representation of the $\sqrt{13} \times \sqrt{13}$ modulation found for 1T-MX_2 with d^1 ions.

p-block bands are affected by the clustering. Our band electronic structure study[6] of 1T-VTe_2 with ribbon-chain modulation shows that it possesses numerous partially filled bands of strong Te p-orbital character. Thus, in general, the 1T-MTe_2 systems with ribbon-chain modulation are expected to be metals.

C. 1T-MX_2 Layers of d^1 Ions. The above discussion shows that, for the MX_2 systems containing d^3, d^2, and $d^{4/3}$ ions, the d-electron-count dependence of their structural modulations can be explained by using either the concept of hidden nesting or the concept of local chemical bonding. This is not the case for the MX_2 layers containing d^1 ions.

With the d^1 electron count, the three 1D bands become each one-sixth-filled (Figure 6b) if they share electrons equally. Alternatively, two 1D bands can become each one-fourth-filled (Figure 6g) if the remaining 1D band is empty. None of these can explain the $\sqrt{13} \times \sqrt{13}$ modulation pattern of Figure 13, because this clustering requires 1D bands of occupancy $f = 1/\sqrt{13}$ ($\approx$0.2774) if it were caused by hidden nesting. From the calculated Fermi surfaces for an undistorted structure of 1T-TaX_2 (X = S or Se), one can only find a partial nesting (e.g., $\mathbf{q} \simeq 0.31\mathbf{a}^*$ in Figure 4b),[22] which is not quite satisfactory in explaining the $\sqrt{13} \times \sqrt{13}$ clustering. As first suggested by Haas,[23] therefore, this clustering may simply originate from local chemical bonding. In the next section, we discuss the $\sqrt{13} \times \sqrt{13}$ clustering in terms of the linear multicenter σ-bonding interactions (e.g., **3c**) involving the in-plane t_{2g} orbitals.

5. Clustering and Linear Multicenter σ-Bonding

Each $\sqrt{13} \times \sqrt{13}$ cluster contains three types of metal atoms (i.e., I, II, and III) as depicted in **4**.[24] The metal atoms I and II form a $\sqrt{7} \times \sqrt{7}$ cluster **5**. This smaller cluster is found in

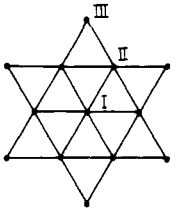

4

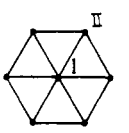

5

the $\sqrt{7} \times \sqrt{7}$ modulation structure of VSe_2.[25] Other kinds of metal-atom clustering reported in the literature are the 4×4 structure of VSe_2 and the $\sqrt{19} \times \sqrt{19}$ structure of $NbTe_2$.[25] All

(22) For other theoretical studies, see: (a) Woolley, A. M.; Wexler, G. *J. Phys. C: Solid State Phys.* **1977**, *10*, 2601. (b) Smith, N. V.; Kevan, S. D.; DiSalvo, F. J. *J. Phys. C: Solid State Phys.* **1985**, *18*, 3175. (c) For an extensive review, see ref 7.

(23) (a) Haas, C. *Solid State Commun.* **1978**, *26*, 709. (b) Haas, C. *J. Solid State Chem.* **1985**, *57*, 82.

(24) Brouwer, R.; Jellinek, F. *Physica B* **1980**, *99*, 51.

(25) van Landuyt, J.; Wiegers, G. A.; Amelinckx, S. *Phys. Status Solidi A* **1978**, *46*, 479.

these structures of metal-atom clustering have the $\sqrt{7} \times \sqrt{7}$ cluster as a common component. As described earlier, strong metal–metal bonding in a 1T-MX_2 layer is achieved by the σ-bonding interactions of the in-plane t_{2g} orbitals, and these interactions occur along each of the three edge-sharing octahedral chain directions of the layer. Thus, the $\sqrt{13} \times \sqrt{13}$ metal-atom clustering may be described as a superposition of linear multicenter σ-bonding interactions occurring independently in three different directions around metal atoms. In the following, we show this to be the case by analyzing the t_{2g}-block electronic structure of the $\sqrt{13} \times \sqrt{13}$ cluster found in 1T-$TaSe_2$.

A. Low-Lying t_{2g}-Block Levels of a $\sqrt{13} \times \sqrt{13}$ Cluster. Let us first examine the essential qualitative features expected for the t_{2g}-block energy levels of the $\sqrt{7} \times \sqrt{7}$ cluster **5**. The central atom of this cluster is engaged in three separate linear, three-center σ-bonding interactions with the peripheral atoms ("radial" interaction). In addition to being a partner of one linear, three-center σ-bonding interaction with the central atom, each peripheral atom of the cluster makes two separate two-center σ-bonding interactions with the adjacent peripheral atoms ("tangential" interaction). The molecular orbitals appropriate for the two-center tangential σ-interactions are **2a**,**b**, and those for the linear, three-center radial σ-interactions are **3a**–**c**. Neglecting the problem of symmetry adaptation, we can regard the t_{2g}-block energy structure of the $\sqrt{7} \times \sqrt{7}$ cluster as being composed of three three-center radial bonding levels **3a**, six two-center tangential bonding levels **2a**, three three-center radial nonbonding levels **3b**, etc., as illustrated in Figure 14a. [The energy levels of Figure 14a were obtained by performing EHMO calculations for the dimer unit Ta_2Se_{10} (**6**) and the trimer unit Ta_3Se_{14} (**7**), which we construct from regular $TaSe_6$ octahedra by edge-sharing.]

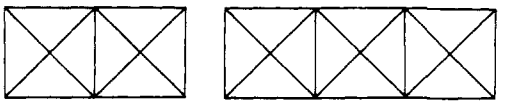

6 7

Figure 14b shows the t_{2g}-block energy levels obtained by EHMO calculations for the $\sqrt{7} \times \sqrt{7}$ cluster, Ta_7Se_{24}, which results from the $\sqrt{13} \times \sqrt{13}$ cluster of 1T-$TaSe_2$ when the outer six Ta(III)Se_6 octahedra are truncated, and Figure 14c represents those for the $\sqrt{13} \times \sqrt{13}$ cluster, $Ta_{13}Se_{42}$. In terms of the major orbital character, the energy levels of Figure 14a–c are correlated as indicated by the arrows. The bottom nine levels of the $\sqrt{13} \times \sqrt{13}$ cluster are closely related to those of the $\sqrt{7} \times \sqrt{7}$ cluster, which are essentially derived from the three radial three-center σ-bonding levels **3a** and six tangential two-center σ-bonding levels **2a**.

In energy, the bottom nine levels of the $\sqrt{13} \times \sqrt{13}$ cluster are lower-lying than those of the $\sqrt{7} \times \sqrt{7}$ cluster. This arises from the fact that the t_{2g} levels of the Ta(III)Se_6 octahedron lie higher in energy than those of the Ta(I)Se_6 or Ta(II)Se_6 octahedra (see Figure 15), which is a direct consequence of the differences in the extent of their octahedral distortions, and hence act *only* as acceptor orbitals. The bottom seven levels of the $\sqrt{13} \times \sqrt{13}$ cluster are particularly low in energy, even lower than the bottom of the levels resulting from the six **2a** orbitals in the $\sqrt{7} \times \sqrt{7}$ cluster. Thus for the 1T-MX_2 layer containing d^1 ions, the formation of the $\sqrt{13} \times \sqrt{13}$ clusters is energetically favorable, because each $\sqrt{13} \times \sqrt{13}$ cluster has 13 electrons for its t_{2g}-block levels so that only the seven low-lying levels are filled.

When the $\sqrt{13} \times \sqrt{13}$ clusters are ordered as shown in Figure 13, one observes the commensurate CDW vector, $1/\sqrt{13}\ a^* = 0.2774a^*$. Experimentally, on lowering the temperature, the 1T-MX_2 phases with d^1 ions show a modulation with incommensurate CDW vector (e.g., $0.283a^*$) before it enters the commensurate CDW state.[1,2] In terms of the chemical bonding picture, the occurrence of the incommensurate CDW vector greater than the commensurate value can be explained if some kinds of kinks smaller in size than the $\sqrt{13} \times \sqrt{13}$ cluster (e.g., the $\sqrt{7} \times \sqrt{7}$ cluster) are included in the ordering of the $\sqrt{13} \times \sqrt{13}$ clusters.

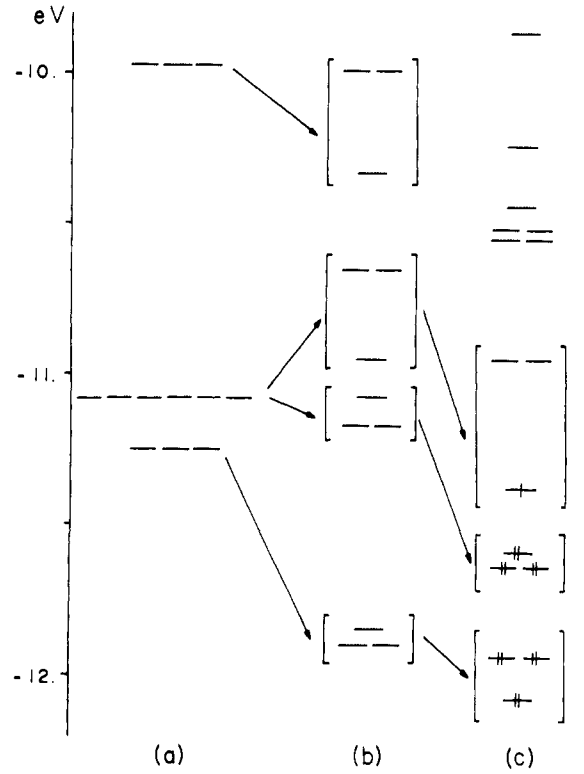

Figure 14. Low-lying t_{2g}-block levels of the $\sqrt{13} \times \sqrt{13}$ cluster unit of 1T-$TaSe_2$ with the $\sqrt{13} \times \sqrt{13}$ modulation: (a) Low-lying t_{2g}-block levels expected for the $\sqrt{7} \times \sqrt{7}$ portion (**5**) of the $\sqrt{13} \times \sqrt{13}$ cluster unit (**4**). These levels were derived from EHMO calculations on the metal dimer (**6**) and the trimer (**7**) units. The bottom three levels are three-center σ-bonding **3a**, the middle six levels are two-center σ-bonding **2a**, the top three are three-center nonbonding **3b**. (b) Low-lying t_{2g}-block levels of the $\sqrt{7} \times \sqrt{7}$ portion (**5**) of the $\sqrt{13} \times \sqrt{13}$ cluster unit (**4**) obtained by EHMO calculations on Ta_7Se_{24}. (c) Low-lying t_{2g}-block levels of the $\sqrt{13} \times \sqrt{13}$ cluster unit (**4**) obtained by EHMO calculations on $Ta_{13}Se_{42}$.

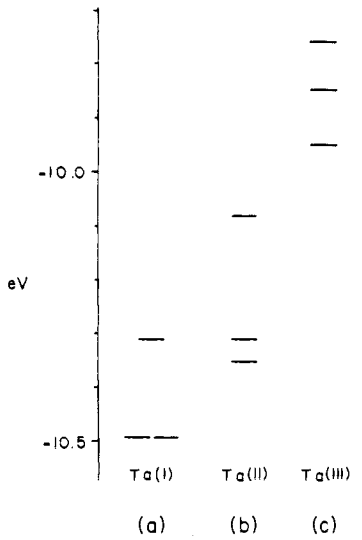

Figure 15. t_{2g}-block levels of the Ta(I)Se_6, Ta(II)Se_6, and Ta(III)Se_6 octahedral units of 1T-$TaSe_2$ with the $\sqrt{13} \times \sqrt{13}$ modulation.

B. t_{2g}-Block Bands of a 1T-MX_2 Layer with $\sqrt{13} \times \sqrt{13}$ Modulation. The HOMO of the $\sqrt{13} \times \sqrt{13}$ cluster is singly filled (Figure 14c), and its main orbital component comes from the tangential orbitals **2a** of the Ta(II) atoms. Namely, in the HOMO of the $\sqrt{13} \times \sqrt{13}$ cluster, the orbital contributions of the peripheral Ta(III)Se_6 octahedra are small. Consequently, in the MX_2 layer with the $\sqrt{13} \times \sqrt{13}$ modulation, the HOMO–HOMO orbital interactions between the $\sqrt{13} \times \sqrt{13}$ clusters are very weak so that the width of the resulting half-filled band is

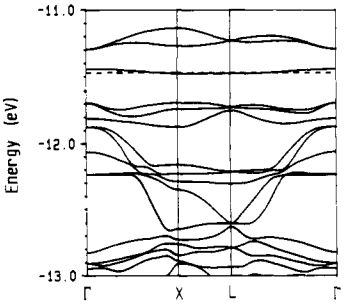

Figure 16. Dispersion relations of the bottom portion of the t_{2g}-block bands calculated for a single 1T-$TaSe_2$ layer with the $\sqrt{13} \times \sqrt{13}$ modulation. The dashed line refers to the Fermi level.

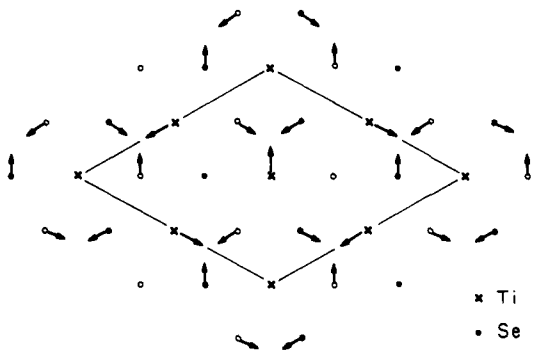

Figure 17. Schematic representation of the 2 × 2 modulated structure of 1T-$TiSe_2$.

very small. This is verified in Figure 16, which shows the dispersion relations of the bottom portion of the t_{2g}-block bands calculated for a single $TaSe_2$ layer of 1T-$TaSe_2$ with the $\sqrt{13} \times \sqrt{13}$ modulation. Thus, in the 1T-MX_2 layers with the $\sqrt{13} \times \sqrt{13}$ modulation, electrons in the half-filled band may be susceptible to localization, as found for 1T-TaS_2.[26]

6. Occurrence of a 2 × 2 Modulation in 1T-$TiSe_2$

1T-TiS_2 is a semiconductor and shows no structural modulation.[27] 1T-$TiSe_2$ is a semimetal and exhibits a 2 × 2 structural modulation, shown in Figure 17, below 202 K.[28] 1T-$TiTe_2$ is also a semimetal and shows anomalies in the temperature dependence of the magnetic susceptibility and specific heat at about 150 K.[29] The latter are indicative of a CDW instability, but no CDW modulation has been detected by X-ray diffraction measurements. In the distortion pattern of Figure 17, there are two kinds of Ti environments. In each Ti(I)Se_6 octahedron (**8**), Ti(I) moves closer to one Se–Se edge of the octahedron, while, in each Ti(II)Se_6 octahedron (**9**), there is no Ti–Se bond shortening but there occurs a rotation between the two Se_3 triangular faces.

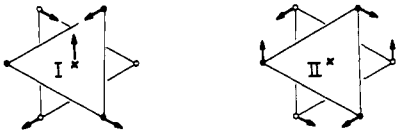

8 **9**

A. Fermi Surface Nesting and 3-Fold Rotational Motion of TiX_6 Octahedra. Unlike the case of 1T-$TiTe_2$, the extent of overlap between the chalcogen p-block and metal d-block bands is not very significant in 1T-$TiSe_2$, so that the amount of the chalcogen-to-metal electron transfer is small.[6] The Fermi surface of 1T-$TiSe_2$ consists of two hole pockets of nearly equal size at Γ (from the partially empty p-block bands) and the electron pockets at L and its equivalent points (from the partially filled d-block band).[27] Thus, the hole pockets at Γ are different in size from the electron pockets at L and its equivalent points. Consequently, a Fermi surface nesting is unlikely to be the cause for the 2 × 2 modulation. In addition, the amount of chalcogen-to-metal electron transfer is larger for 1T-$TiTe_2$ (to the extent that it makes the d-electron count close to $d^{1/3}$)[6] than it is for 1T-$TiSe_2$, so that the Fermi surface area is greater in 1T-$TiTe_2$ than it is in 1T-$TiSe_2$. Thus, the idea of Fermi surface nesting incorrectly predicts that 1T-$TiTe_2$ has a greater tendency for structural modulation.

The three lowest-lying d-block levels of an ideal MX_6 octahedron are degenerate, while they are split in a one-below-two pattern in an ideal MX_6 trigonal prism (Figure 18). The distortion of **9** is a 3-fold rotational motion of the Ti(II)Se_6 octahedron toward a trigonal prism. Therefore, Hughes[30] proposed that the 3-fold rotational motion of the Ti(II)Se_6 is energy-lowering (because the t_{2g}-block bands of 1T-$TiSe_2$ are partially filled, though very slightly) and hence causes the structural modulation. Because 1T-$TiTe_2$ has a greater amount of chalcogen-to-metal electron transfer than does 1T-$TiSe_2$, more electrons are present in the t_{2g}-block bands of 1T-$TiTe_2$. Thus, Hughes's suggestion leads to an incorrect prediction that 1T-$TiTe_2$ has a greater tendency for structural modulation than does 1T-$TiSe_2$.

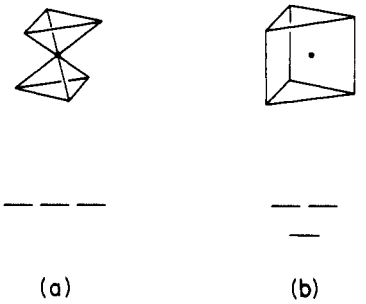

Figure 18. Three low-lying d-block levels of (a) an MX_6 octahedron and (b) an MX_6 trigonal prism.

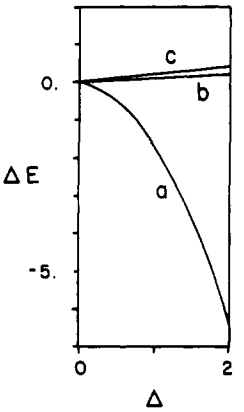

Figure 19. Relative energy ΔE (kcal/mol) of $TiSe_6^{8-}$ octahedron calculated as a function of the reaction coordinate Δ for (a) mode a, (b) mode b, and (c) mode c.

B. Second-Order Jahn–Teller Instability. We now show that the structural modulation of 1T-$TiSe_2$ originates from the energy lowering associated with the Ti–Se bond shortening in the Ti(I)Se_6 octahedra (**8**) by studying the electronic structure of an $TiSe_6^{8-}$ (with d^0 ion) octahedron. For convenience, we define the reaction coordinate Δ that gradually converts an undistorted $TiSe_6$ structure (Δ = 0) to the distorted Ti(I)Se_6 and Ti(II)Se_6 structures (Δ = 1). As an undistorted $TiSe_6$ structure, we employ the one with D_{3d} symmetry derived from the undistorted 1T-$TiSe_2$ structure. The energetics associated with the octahedral distortions are examined by performing EHMO calculations for $TiSe_6^{8-}$ on the

(26) (a) Tosati, E.; Fazekas, P. *J. Phys. (Paris)* **1976**, *37*, C4-165. (b) Dardel, B.; Grioni, M.; Malterre, D.; Weibel, P.; Baer, Y.; Lévy, F. *Phys. Rev. B* **1992**, *45*, 1462.
(27) Wilson, J. A. *Phys. Status Solidi B* **1978**, *86*, 11.
(28) DiSalvo, F. J.; Moncton, D. E.; Waszczak, J. V. *Phys. Rev. B* **1976**, *14*, 4321.
(29) de Boer, D. K. G.; van Bruggen, C. F.; Bus, G. W.; Coehoorn, R.; Haas, C.; Sawatzky, G. A.; Myron, H. W.; Norman, D.; Padmore, H. *Phys. Rev. B* **1984**, *29*, 6797.
(30) Hughes, H. P. *J. Phys. C: Solid State Phys.* **1977**, *10*, L319.

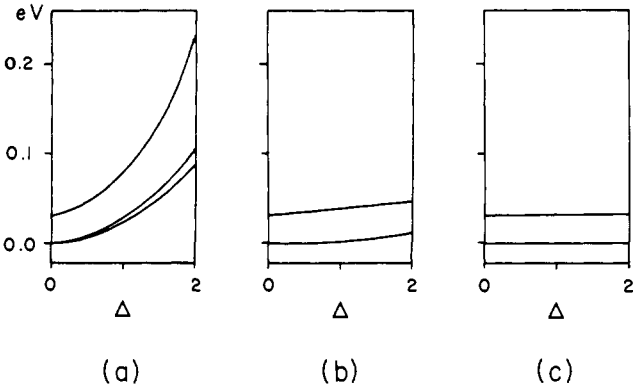

Figure 20. Variation of the t_{2g}-block levels of $TiSe_6$ octahedron calculated as a function of the reaction coordinate Δ for (a) mode a, (b) mode b, and (c) mode c.

basis of three distortion modes. (a) Mode a, both the Ti and the Se atoms move gradually to form the Ti(I)Se_6; (b) mode b, only the Se atoms move gradually as in the Ti(I)Se_6 structure; and (c) mode c, the Se atoms move gradually to form the Ti(II)Se_6 structure. Note that shortening of Ti–Se bonds occurs in mode a, only very weakly in mode b, but not at all in mode c. In modes b and c, there occurs a shortening of some Se···Se contacts. The energies of $TiSe_6^{8-}$ calculated as a function of Δ for the three modes of distortion are summarized in Figure 19, which reveals that only mode a is energetically favorable. Consequently, it is the shortening of the Ti–Se bonds in the Ti(I)Se_6 octahedra that is crucial in stabilizing the modulated structure of 1T-$TiSe_2$. The slight shortening of some Se···Se contacts in both Ti(I)Se_6 and Ti(II)Se_6 does not play any important role in stabilizing the modulated structure.

Figure 20 shows the t_{2g}-block levels of $TiSe_6^{8-}$ calculated as a function of Δ for the three modes of distortion. As the distortion progresses, these levels are considerably raised in energy for mode a while they remain nearly constant for modes b and c. This reflects the fact that the nature of the interaction between Ti and Se is antibonding in the t_{2g}-block levels (see **10**). Thus, the total

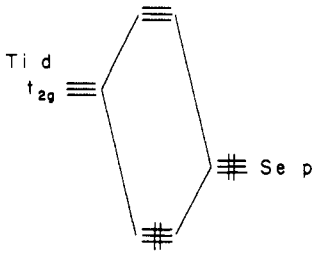

10

energy lowering given by distortion mode a means that the Ti–Se bond shortening in the Ti(I)Se_6 octahedra enhances the role of the Ti d orbitals as acceptor levels in lowering the energies of the Ti–Se bonding levels. In molecular chemistry terminology, the distortion of the Ti(I)Se_6 octahedra is a second-order Jahn–Teller distortion.[8b] In short, the energy lowering that gives rise to the structural modulation of 1T-$TiSe_2$ does not occur in the t_{2g}-block bands but in the Se p-block bands.

C. Absence of a 2 × 2 Modulation in 1T-TiX_2 (X = S or Te). Our conclusion that the structural modulation of 1T-$TiSe_2$ is essentially caused by a second-order Jahn–Teller instability provides a natural explanation for why a similar modulation does not occur in 1T-TiX_2 (X = S or Te). The bottom portion of the t_{2g}-block bands is more occupied in 1T-$TiTe_2$[29] than in 1T-$TiSe_2$[31] due to the greater amount of chalcogen-to-metal electron transfer in 1T-$TiTe_2$. Therefore, a distortion such as **8** in the 1T-$TiTe_2$ lattice would be energetically unfavorable because more filled d-block energy levels are raised in energy. To achieve a second-order Jahn–Teller distortion, the electronic energy gain associated with the mixing of two different energy levels must overcome the strain associated with the distortion. Thus a favorable situation occurs when a small movement of atoms can cause a large change in overlap integrals. Since the orbitals of S are more contracted than those of Se, the tendency for a second-order Jahn–Teller distortion such as **8** is expected to be weak in 1T-TiS_2. In terms of this factor alone, 1T-$TiTe_2$ should have a stronger tendency for distortion because the orbitals of Te are more diffuse than those of Se. However, this very diffuseness of the Te orbitals is responsible for the large amount of chalcogen-to-metal electron transfer,[6] which diminishes the tendency for a second-order Jahn–Teller distortion.

7. 3 × 3 Modulation of 2H-MX_2 (M = Nb, X = Se; M = Ta, X = S or Se)

As a final topic of the present work, we examine the 3 × 3 modulation (with vectors $\mathbf{q}_a = \mathbf{a}^*/3$ and $\mathbf{q}_b = \mathbf{b}^*/3$) observed for the 2H-$MX_2$ (M = Nb, X = Se; M = Ta, X = S or Se) phases containing d^1 ions.[1,2,24,32] These compounds consist of MX_2 layers made up of MX_6 trigonal prisms by sharing the edges of their rectangular faces (Figure 21a). If the structure of an undistorted 2H-MX_2 layer is represented by an array of metal ions as shown in Figure 21b, then the metal-ion distortion patterns proposed by Moncton et al.[32] and by Brouwer and Jellinek[24] for the 3 × 3 modulation can be represented as in Figure 21c (model a) and Figure 21d (model b), respectively. The cluster modes a and b differ in the choice of the metal atom displacement directions. In this section, we study the electronic structures of both the undistorted[33] and the distorted TaS_2 layers by performing EHTB calculations in order to find how the occurrence of the 3 × 3 modulation can be understood.

A. d-Block Bands of an Undistorted 2H-TaS_2 Layer. Figure 22a shows the dispersion relations of the three lowest-lying d-block bands calculated for a single TaS_2 layer of undistorted 2H-TaS_2 by employing the EHTB method. The Fermi surface associated with the half-filled band of Figure 22a is shown in Figure 22b. The essential features of this band electronic structure are very close to those obtained by first-principles calculations.[7] As already noted by others, the nearly circular pockets of the calculated Fermi surface are well nested. However, two of the nesting vectors associated with these pockets are perpendicular to the a^*- and b^*-directions, while the remaining one is perpendicular to the $(-a^* + b^*)$-direction. The nearly hexagonal pocket centered at Γ has nesting vectors close to $\mathbf{a}^*/2$, $\mathbf{b}^*/2$, and $(-\mathbf{a}^* + \mathbf{b}^*)/2$. Thus, both sets of nesting vectors differ from the observed modulation vectors $\mathbf{a}^*/3$ and $\mathbf{b}^*/3$, so that Fermi surface nesting cannot be the cause for the 3 × 3 modulation.

B. Nature of the Half-Filled Band. Commonly, the half-filled band of Figure 22a is referred to as the "z^2" band, but it has a strong contribution from the $x^2 - y^2$ and xy orbitals as found by various calculations.[34] Recently, Yee and Hughbanks[34a] examined the metal–metal bonding interactions leading to the z^2 band of a 2H-MX_2 type material by employing semilocalized bonding schemes. This approach provides an elegant explanation for why the hydrogen atoms of the H_xMS_2 (M = Nb or Ta) bronzes are located in the triangular interstices within the metal layers.[35] For the purpose of probing the electronic factor responsible for the 3 × 3 modulation of the d^1 2H-MX_2 layer in the next section, we will first examine the nature of the z^2 band (hereafter, referred to as the half-filled band) in some detail.

The orbital composition of the half-filled band is first examined by calculating the contributions of the metal z^2, $x^2 - y^2$, and xy orbitals to the total density of states (DOS) (i.e., the partial DOS).

(31) Anderson, O.; Manzke, R.; Skibowski, M. *Phys. Rev. Lett.* **1985**, *55*, 2188.

(32) Moncton, D. E.; Axe, J. D.; DiSalvo, F. J. *Phys. Rev. B* **1977**, *16*, 801.

(33) Meetsma, A.; Wiegers, G. A.; Haange, R. J.; de Boer, J. L. *Acta Crystallogr.* **1990**, *C46*, 1598.

(34) (a) Yee, K. A.; Hughbanks, T. *Inorg. Chem.* **1991**, *30*, 2321. (b) For a review, see ref 7.

(35) (a) Riekel, C.; Reznik, H. G.; Schöllhorn, R.; Wright, C. J. *J. Chem. Phys.* **1979**, *70*, 5203. (b) Kleinberg, R. L.; Jacobsen, A. J.; Silbernagel, B. G.; Halbert, T. R. *Mater. Res. Bull.* **1980**, *15*, 1541.

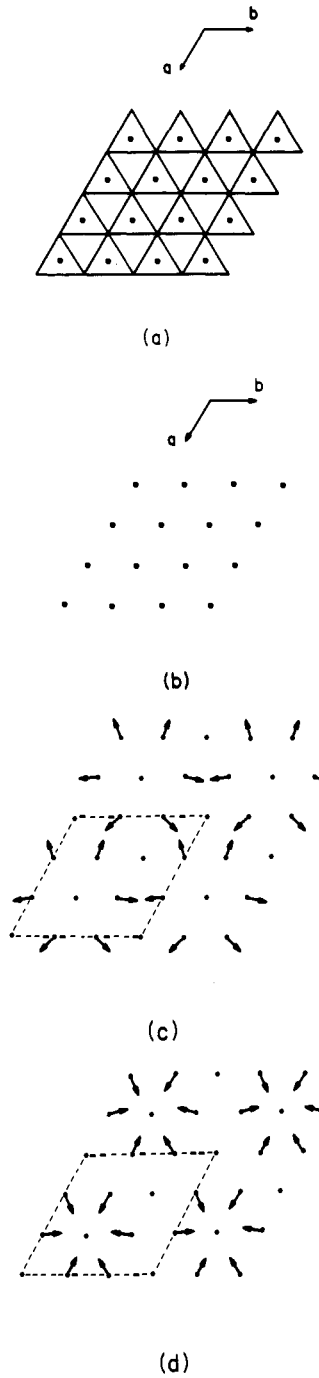

Figure 21. (a) Schematic projection view of an undistorted 2H-MX_2 layer along the *c*-direction (perpendicular to the layer). (b) Metal ion arrangement in an undistorted 2H-MX_2 layer. (c) 3 × 3 clustering of metal atoms in 2H-MX_2 with d^1 ions proposed by Moncton et al (model a).[32] (d) 3 × 3 clustering of metal atoms in 2H-MX_2 with d^1 ions proposed by Brouwer and Jellinek (model b).[24]

Table I. Relative Stabilization Energies[a] Calculated for a Single 2H-TaS_2 Layer as a Function of the Metal Atom Displacement δ[b]

d	model a	model b
0.000	0.00	0.00
0.050	0.39	0.43
0.075	0.44	0.53
0.100	0.46	0.63

[a] In kcal/mol per TaS_2 unit. [b] In angstroms.

Figure 23a shows the partial DOS calculated for the z^2 and that for the $x^2 - y^2/xy$ orbitals. Each of these partial DOS plots peaks near the bottom of the band, and the sum of the $x^2 - y^2/xy$ orbital contributions is somewhat greater than the z^2 orbital contribution.

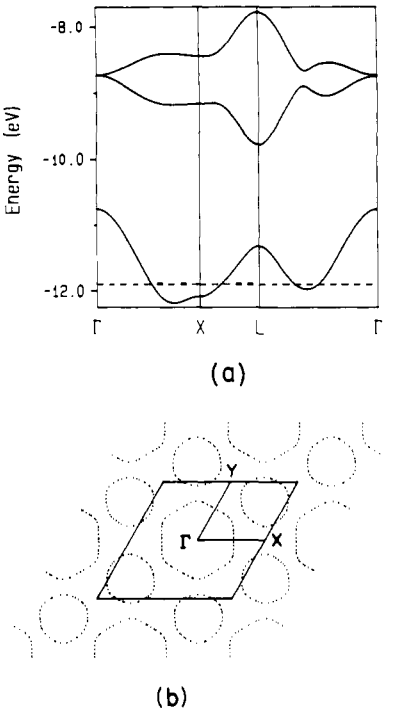

Figure 22. (a) The three lowest-lying d-block bands calculated for an undistorted 2H-TaS_2 layer. The dashed line refers to the Fermi level. Γ = (0, 0), X = ($a^*/2$, 0), and L = ($a^*/3$, $b^*/3$). (b) Fermi surface associated with the half-filled band of the undistorted 2H-TaS_2 layer. Γ = (0, 0), X = ($a^*/2$, 0), and Y = (0, $b^*/2$).

The nature of the half-filled band is examined further by analyzing its orbital character at the special wave vector points Γ, X, Y, and M of the FPZ (see Figure 3b). At Γ, each trigonal prism has the orbital **11a**, which can be represented by a projection view

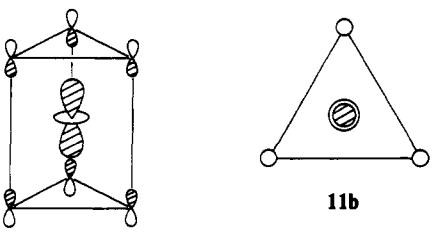

11a **11b**

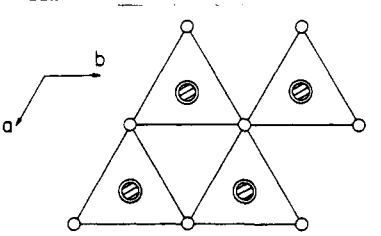

12

11b. Then, the crystal orbital at Γ is given by **12**. By symmetry, the $x^2 - y^2$ and xy orbitals do not mix into the crystal orbital at Γ. The z^2 orbitals are perpendicular to the layer, so that metal–metal bonding interactions do not occur at Γ. At X, each trigonal prism has the orbital **13a**, which can be represented by a projection view **13b**. Then, the crystal orbital at X is given by **14**. The orbital at each metal center is a hybrid of z^2, $x^2 - y^2$, and xy orbitals elongated along the *b*-direction, and these hybrid metal orbitals make σ-bonding interactions along that direction. The out-of-phase arrangement between these orbitals along the *a*-direction has no significant consequence because the hybrid orbitals are not aligned along that direction. This explains why the energy of the half-filled band is lower in energy at X than at Γ (Figure 22a). In a similar manner, the crystal orbital at Y is given by **15**, in which the metal hybrid orbitals elongated along

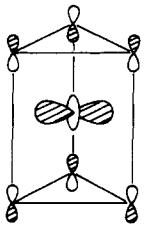

13a

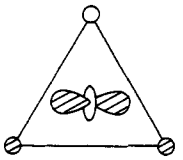

13b

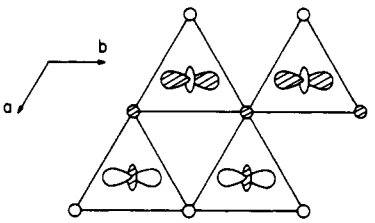

14

the a-direction make σ-bonding interactions along that direction. Likewise, the crystal orbital at M is given by **16**, in which the metal hybrid orbitals elongated along the $(a + b)$-direction make σ-bonding interactions along that direction.

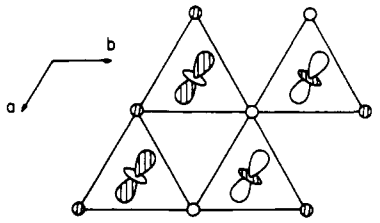

15

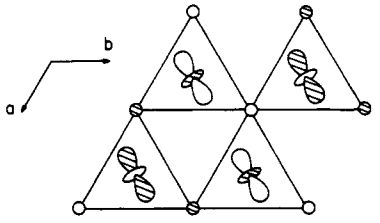

16

Thus, as far as the half-filled band of a d^1 2H-MX_2 layer is concerned, metal–metal bonding interactions occur equally well along the a-, b-, and $(a + b)$-directions. The metal orbitals responsible for these interactions are the hybrid orbitals (made up of the z^2, $x^2 - y^2$ and xy orbitals) elongated along the a-, b-, and the $(a + b)$-directions, i.e., the metal–metal directions.

C. Metal–Metal Bonding and 3 × 3 Modulation. According to the orbital nature of the half-filled band, the 3 × 3 modulated structure of a d^1 2H-MX_2 layer suggests that the extent of the overall metal–metal bonding interactions of the layer is enhanced by the shortening of some metal–metal distances associated with the modulation. To examine the energetics associated with the distortion leading to the 3 × 3 modulated structures shown in Figure 21c,d, we carry out EHTB calculations for a single 2H-TaS_2 layer with 3 × 3 modulation. To simplify our calculations, the clustering patterns of model a (Figure 21c)[32] and model b[24] (Figure 21d) are simulated by displacing the appropriate metal atoms from their positions in the undistorted structure, while keeping the S atom positions fixed. This approximation is reasonable in view of the experimental finding that the displacement of Se is much smaller than that of Ta in 2H-$TaSe_2$.[32] The magnitudes of the metal-atom displacement, δ, used in our calculations are 0.050, 0.075, and 0.100 Å. (Note that the δ value of 0.050 Å is close to the experimental value.)[32] Table I summarizes the relative stabilization energies, in kcal/mol per TaS_2 unit, calculated as a function of δ for the 2H-TaS_2 layers with the distortion patterns of models a and b. With both models, the

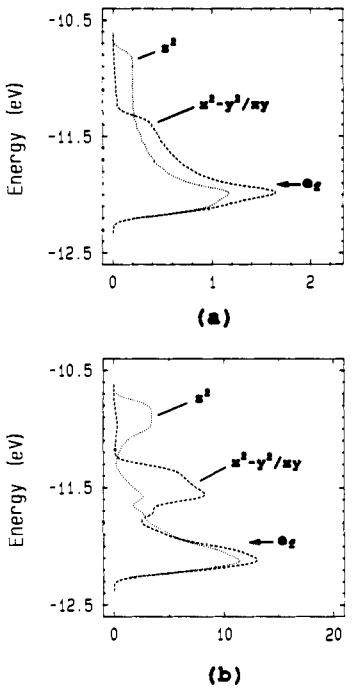

Figure 23. (a) Partial DOS of the z^2 orbital (dotted line) and that of the $x^2 - y^2/xy$ orbitals (dashed line), in units of electrons per unit cell, calculated for the undistorted 2H-TaS_2 layer. For simplicity, only the energy window covering the half-filled band of Figure 22a was used. (b) Partial DOS of the z^2 orbital (dotted line) and that of the $x^2 - y^2/xy$ orbitals (dashed line), in units of electrons per unit cell, calculated for the distorted 2H-TaS_2 layer with the 3 × 3 modulation based on the clustering model b (δ = 0.05 Å). The energy window used is the same as that in Figure 23a. The unit cell of the 3 × 3 modulated structure is 9 times that of the undistorted structure. Thus the partial DOS plot of part b was reduced in scale by 9 times so that it could be directly compared with the partial DOS plot of part a given for the unit cell size of TaS_2.

modulated structures are calculated to be more stable than the undistorted structure. For a given displacement, models a and b provide similar stabilization energies for all practical purposes although model b is very slightly more favorable. The stabilization energy of 0.4 kcal/mol per TaS_2 unit calculated for δ = 0.05 Å corresponds to a thermal energy (i.e., k_BT) of 200 K, which seems quite reasonable because the 3 × 3 modulation of 2H-TaS_2 begins to appear at 75 K[1,2] when the temperature is lowered.

Table II summarizes the overlap populations calculated for the various nearest-neighbor metal–metal contacts found in the undistorted and the distorted structures (models a and b with δ = 0.050 Å) of a single 2H-TaS_2 layer. In both the undistorted and distorted structures, all nearest-neighbor metal–metal contacts have a positive overlap population. This arises from the electron-deficient nature of the 2H-MX_2 systems with d^1 ions; namely, there are not enough electrons to fill all the d-block levels possessing metal–metal bonding character. Compared with the case of the undistorted structure, the metal–metal contacts shortened by the modulation have an increased overlap population and the lengthened ones a decreased value. On the average, however, the overlap population per metal–metal bond is found to increase slightly by the modulation, which is consistent with the finding that the total energy is lowered by the modulation.

Figure 23b shows the partial DOS of the z^2 orbital and those of the $x^2 - y^2/xy$ orbitals calculated for a single 2H-TaS_2 layer with the 3 × 3 modulation (based on the metal clustering model a and δ = 0.050 Å). The partial DOS peak for the $x^2 - y^2/xy$ orbitals is split into two subpeaks. The lower subpeak is associated with the shortened metal–metal contacts and the upper subpeak with the lengthened metal–metal contacts. It is noteworthy that the Fermi level of this modulated structure lies just at the top of the lower subpeak. This means that 2H-MX_2 layers with d^1 ions have enough electrons to fill only the energy levels stabilized by

Table II. Distances[a] and Overlap Populations (O.P.) Calculated for the Ta–Ta Contacts in the Undistorted 2H-TaS_2 Layer and the Distorted 2H-TaS_2 Layers with the 3 × 3 Modulations (Models a and b with Displacement δ = 0.05 Å)

undistorted		distorted			
		model a		model b	
distance	O.P.	distance	O.P.	distance	O.P.
3.314 (×27)	0.0692	3.214 (×3)	0.0995	3.264 (×12)	0.0882
		3.289 (×12)	0.0793	3.339 (×12)	0.0594
		3.364 (×12)	0.0544	3.414 (×3)	0.0444

[a] In angstroms.

Table III. Onset Temperatures (T_0)[37] for the $\sqrt{13} \times \sqrt{13}$ Modulations of 2H-MX_2 and the 3 × 3 Modulations of 1T-MX_2

2H-MX_2	T_0 (K)	1T-MX_2	T_0 (K)
2H-TaS_2	~80	1T-TaS_2	~600
2H-$TaSe_2$	122	1T-$TaSe_2$	~600
2H-$NbSe_2$	32	1T-VSe_2	112

the modulation (i.e., those representing the shortened metal–metal contacts), which is therefore energetically most favorable.

D. Comparison between 2H-MX_2 and 1T-MX_2 Layers with d^1 Ions. Since the bottom d-block band of an undistorted 2H-MX_2 layer is half-filled (with d^1 ions at the metal positions), one might expect some kind of dimerization such as **17** on the basis of the two-center two-electron bonding idea. However, it should be noted

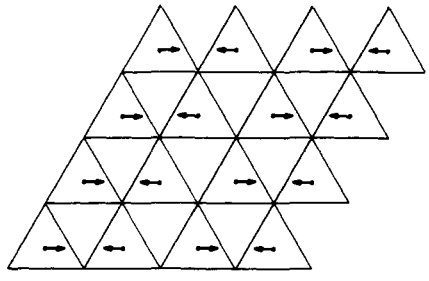

17

that this band is composed of three d orbitals, i.e., z^2, $x^2 - y^2$, and xy. In a sense, one electron of each metal ion is shared among the three d orbitals. From this viewpoint, the electronic structure of 2H-MX_2 with d^1 ions is analogous to that of 1T-MX_2 with d^1 ions in which one electron is shared among the three t_{2g}-block orbitals. Thus, as in the case of the 1T-MX_2 phases with d^1 ions, the 2H-MX_2 compounds with d^1 ions are electron-deficient systems. For such systems, the formation of the metal cluster preserving the local trigonal symmetry of the lattice is energetically more favorable than the formation of two-center, two-electron bonds destroying the trigonal symmetry.

Table III summarizes the onset temperatures (T_0's) for the 3 × 3 structural modulations of 2H-MX_2 and the $\sqrt{13} \times \sqrt{13}$ modulations of 1T-MX_2. The T_0 of 1T-TaX_2 is much higher than that of 2H-TaX_2 (X = S or Se) thereby indicating that the tendency for the metal-atom clustering is much stronger for 1T-TaX_2 than for 2H-TaX_2. This is reasonable because the octahedral coordination of 1T-MX_2 provides much stronger metal–metal bonding interactions than does the trigonal-prismatic coordination of 2H-MX_2. The T_0 is higher for 2H-$TaSe_2$ than for 2H-$NbSe_2$ and is higher for 2H-$TaSe_2$ than for 2H-TaS_2. Namely, in 2H-MX_2, the T_0 is raised when either the lower-row metal or the lower-row chalcogen atom is used. The lower-row metal has more extended d-orbitals and hence provides a substantial change in overlap for a small distortion. The lower-row chalcogen is more polarizable. Both factors help reduce the extent of lattice strain that the structural modulation induces thereby explaining the above observation for the 2H-MX_2 systems. The T_0 values of the 1T-MX_2 systems exhibit a similar trend. [Experimental uncertainties exist for the T_0 values of 1T-TaS_2 and 1T-$TaSe_2$. However, the CDW lock-in temperature is higher for 1T-$TaSe_2$ than for 1T-TaS_2 (i.e., 473 vs ~200 K), so that the T_0 value is also likely to be higher for 1T-$TaSe_2$.]

8. Concluding Remarks

A CDW formation associated with a Fermi surface nesting introduces an energy gap at the Fermi level. The molecular analogy[36] of a Fermi-surface-nesting induced CDW formation is a first-order Jahn–Teller instability, i.e., the tendency for a molecule with partially filled degenerate levels to undergo a distortion which lifts the degeneracy. In the present work, we analyzed the d-electron-count dependence of the distortion patterns in 1T-MX_2 phases in terms of the electronic structure of an undistorted 1T-MX_2 layer. It is impossible to explain the d-electron-count dependence of the structural modulations by applying the concept of Fermi surface nesting to the calculated Fermi surfaces of 1T-MX_2.

The structure of an ideal 1T-MX_2 layer can be constructed from edge-sharing octahedral chains. This structural characteristic allows us to approximate the t_{2g}-block bands of the layer as a superposition of contributions from the three sets of edge-sharing chains, thereby giving rise to the hidden 1D Fermi surfaces for the 1T-MX_2 layer, provided that we consider only the strongest interactions of the in-plane t_{2g} orbitals, i.e., the σ-bonding interactions within each edge-sharing octahedral chain. Then, the diamond-chain formation in 1T-MX_2 with d^3 ions is easily explained in terms of the hidden-nesting concept. The zigzag-chain formation in 1T-MX_2 with d^2 ions and the ribbon-chain formation in 1T-MX_2 with $d^{4/3}$ ions are explained in terms of the hidden-nesting concept when the hidden 1D Fermi surfaces are obtained under the assumption that one of the three 1D chain bands is not occupied.

From the viewpoint of local chemical bonding, the driving force for the structural modulations of 1T-MX_2 is two-center, two-electron σ-bonding for the diamond-chain and zigzag-chain formations and three-center, two-electron σ-bonding for the ribbon-chain formation. The $\sqrt{13} \times \sqrt{13}$ cluster formation in 1T-MX_2 with d^1 ions is difficult to understand within the framework of Fermi surface nesting. In terms of local chemical bonding, the $\sqrt{13} \times \sqrt{13}$ clustering is described as a superposition of linear multicenter σ-bonding interactions occurring independently in three different directions around metal atoms. Strong metal–metal bonding is achieved by the σ-interactions of the in-plane t_{2g} orbitals, and these interactions occur along each of the three edge-sharing octahedral chain directions of the layer.

As in the case of the $\sqrt{13} \times \sqrt{13}$ modulations of 1T-MX_2 with d^1 ions, the 2 × 2 modulation of 1T-$TiSe_2$ and the 3 × 3 modulations of 2H-MX_2 containing d^1 ions are also difficult to explain in terms of the Fermi surface nesting concept. Our analysis shows that the 2 × 2 modulation of 1T-$TiSe_2$ results from a second-order Jahn–Teller instability of the $TiSe_6$ octahedra containing d^0 ions, while the 3 × 3 modulation of 2H-MX_2 occurs to enhance the extent of their metal–metal bonding interactions between adjacent MX_6 trigonal prisms. The metal clustering patterns in the $\sqrt{13} \times \sqrt{13}$ modulation of 1T-MX_2 and the 3 × 3 modulation of 2H-MX_2 preserve a local trigonal symmetry, due to their electron deficiency.

It is interesting that the structural modulations of 1T-MX_2 and 2H-MX_2 containing d^1 ions, which helped popularize the concept of Fermi surface nesting, are difficult to understand without the use of local chemical bonding ideas. The Fermi nesting concept is applicable to a situation in which the energy of a system is lowered by opening a band gap at the Fermi level with the help of a structural modulation, i.e., the solid-state analogue of a first-order Jahn–Teller distortion. As established by the Walsh diagram approach,[8b] molecules without partially filled degenerate levels can be susceptible to molecular geometry distortion (e.g., second-order Jahn–Teller distortion). Certainly, the solid-state

(36) (a) Whangbo, M.-H. in ref 4b, p 27. (b) Whangbo, M.-H. *Acc. Chem. Res.* **1983**, *16*, 95. (c) Wheeler, R. A.; Whangbo, M.-H.; Hughbanks, T.; Hoffmann, R.; Burdett, J. K.; Albright, T. A. *J. Am. Chem. Soc.* **1986**, *108*, 2222.

(37) For a review, see: DiSalvo, F. J. In *Electron-Phonon Interactions and Phase Transitions*; Riste, T., Ed.; Plenum: New York, 1977; p 107.

counterpart of this situation cannot be explained in terms of the Fermi surface nesting concept, and the occurrence of a structural modulation in low-dimensional metals does not necessarily originate from a Fermi surface nesting.

On the basis of our finding that analogies exist between the concepts of chemistry and solid-state physics dealing with structural instabilities, one should not neglect one picture over the other. For example, the incommensurate nature of the CDW vectors in the Magnéli phase Mo_4O_{11}, the monophosphate tungsten bronzes, and the blue bronzes $A_{0.33}MoO_3$ (A = K, Rb, or Tl) are easily explained by employing the concept of Fermi surface nesting. On the other hand, why these materials possess 1D-like electronic structures can be easily understood by analyzing the distortion patterns of their MO_6 octahedra.[9b] In general, the concept of Fermi surface nesting allows one to predict the symmetry of the distorted lattice resulting from a CDW instability, but it does not provide a detailed local bonding picture. The opposite is the case with the concepts of local chemical bonding. Thus, the concept of Fermi surface nesting is complementary to that of local chemical bonding.

Acknowledgment. This work was supported by the U.S. Department of Energy, Office of Basic Sciences, Division of Materials Sciences, under Grant DE-FG05-86ER45259, by NATO, Scientific Affairs Division, and by Centre National de la Recherche Scientifique, France.

Solvent Structure around Cations Determined by ^1H ENDOR Spectroscopy and Molecular Dynamics Simulation

M. Sivaraja,[†] T. R Stouch,[‡] and G. C. Dismukes*,[†]

Contribution from the Department of Chemistry, Princeton University, Princeton, New Jersey 08544, and Department of Macromolecular Modelling, Bristol-Myers Squibb, Princeton, New Jersey 08543. *Received July 22, 1991*

Abstract: Classical molecular dynamics simulations of metal ion solvation have been found to confirm the experimental ^1H ENDOR and EPR spectroscopic results on the coordination structure of water molecules surrounding paramagnetic Mn^{2+} ions in frozen aqueous solutions. The well-known simplification and intensification of the six-line Mn^{2+} EPR signal in frozen solutions upon reducing the pH was found to coincide with the appearance of three strong ^1H ENDOR resonances, reflecting symmetrization of the first two solvation shells. From the dipolar part of the hyperfine interaction, the Mn–H distances for the first and second shells were determined to be 2.87 and 4.8 Å, respectively. All protons in the first shell were located at the same distance. Classical molecular dynamics simulations confirmed the experimental distances to both shells using a three-point flexible water model which included electrostatic and van der Waals interactions to Mn^{2+}. At 50 K, the structured second shell of the Mn–H radial distribution function is comprised of 18 water molecules, reflecting disorder which becomes dynamically averaged at 300 K as the second shell expands to encompass on average 22 H_2O molecules at a mean distance of 5.0 Å. The ENDOR and dynamics results support the proposed model of second-shell solvent fluctuation of the Mn^{2+} ligand field splitting as the mechanism for electron spin relaxation of Mn^{2+}. These results should encourage the use of classical molecular dynamics simulations to predict solvation structure of nonparamagnetic ions for which experimental data are not readily available.

This study examines the general question of the solvent structure surrounding metal ions in disordered systems.[1] The absence of long range order makes such systems particularly difficult to study. As a class of matter, disordered systems are extremely common. Specifically, we have choosen Mn^{2+} ions in water because solvation can be measured spectroscopically and modeled theoretically using realistic assumptions. While there are various methods to examine the first-shell solvation structure, the structure of the second shell is difficult to observe by direct methods. An accurate picture of metal ion solvation extending out to the second solvation shell should be obtainable in principle by combining high-resolution electron-nuclear double resonance spectroscopy (ENDOR) and classical molecular dynamics simulations. These tools have not been combined previously to study ion solvation. The ENDOR method enables measurement of the distance between a paramagnetic metal ion and the surrounding solvent nuclei from their ^1H hyperfine interaction.[1,2] Classical molecular dynamics simulations of water solvation, when parametrized with accurate molecular structure and thermodynamic data, can aid in the interpretation of data on intermolecular structure and the dynamics of ion solvation.[3]

Mn^{2+} in aqueous solution exists essentially as the hexaaquo ion at pH below the pK_a (10.5). The stability constants for the complexes with the counterions $[Mn(H_2O)_5X]^+$, Cl^- (0.04 M^{-1}), and ClO_4^- are low, so they are not major species.[4] Evidence for a change in solvation upon freezing is seen in the 10–100-fold reduction in the EPR signal intensity and the broadening of its six-line ^{55}Mn hyperfine structure. This arises from the freezing in of solvent configurations of low symmetry, which removes the 5-fold degeneracy of the spin $S = {}^5/_2$, so called zero-field splitting (ZFS). In fluid solutions, solvent fluctuations tend to average out the static disorder which can be trapped by freezing. The lifetime for water exchange in the first shell in fluid solutions, 2×10^{-7} s, is too slow to dynamically averaged the characteristic ZFS frequencies imposed by low symmetry solvent coordination ($\sim 10^2$–10^4 MHz).[5a] Hence, the first coordination shell must rapidly fluctuate around an equilibrium cubic symmetry. This led to the model postulating that the correlation time for fluc-

[†] Princeton University.
[‡] Bristol-Myers Squibb.

(1) (a) Hutchison, C.; McKay, D. B. *J. Chem. Phys.* **1977**, *66*, 3311. (b) Hurst, G. C.; Henderson, T. A.; Kreilick, R. W. *J. Am. Chem. Soc.* **1985**, *107*, 7294. (c) Yim, M. B.; Makinen, M. W. *J. Magn. Reson.* **1986**, *70*, 89. (d) Mustafi, D.; Makinen, M. *Inorg. Chem.* **1988**, *27*, 3360.
(2) De Beer, R.; De Boer, W.; Van't Hoff, C. A.; Van Ormondt, D. *Acta Crystallogr.* **1973**, *B29*, 1473.
(3) (a) Teleman, O.; Ahlstrom, P. *J. Am. Chem. Soc.* **1986**, *108*, 4333–4341. (b) Chandraskhar, J.; Spellmeyer, D. C.; Jorgensen, W. L. *J. Am. Chem. Soc.* **1984**, *106*, 903–910.
(4) Smith, R. M.; Martell, A. E. *Critical Stability Constants*; Plenum Press: New York, 1976; Vol. 4.
(5) (a) Ducommun, Y.; Newman, K. E.; Merbach, A. E. *Inorg. Chem.* **1979**, *18*, 2754. (b) Martini, G.; Romanelli, M.; Burlamacchi, L. In *Molecular Motions in Liquids*; Lascombe, J., Ed.; Reidel: Dordrecht, 1974; p 371.

0002-7863/92/1514-9600$03.00/0